AAAS
Research
Volume 2021, Article ID 5130420, 30 pages
https://doi.org/10.34133/2021/5130420

Research
A SCIENCE PARTNER JOURNAL

Review Article

Recent Advances in Molybdenum-Based Materials for Lithium-Sulfur Batteries

Henghan Dai,[1] Lumin Wang,[1] Yue Zhao,[1] Jialu Xue,[1] Ruicong Zhou,[1] Chenyang Yu,[1] Jianing An,[2] Jinyuan Zhou,[3] Qiang Chen,[4] Gengzhi Sun,[1,5] and Wei Huang[1,5]

[1]*Institute of Advanced Materials (IAM), Nanjing Tech University (NanjingTech), Nanjing 211816, China*
[2]*Institute of Photonics Technology, Jinan University, Guangzhou 510632, China*
[3]*School of Physical Science and Technology, Lanzhou University, Lanzhou 730000, China*
[4]*School of Materials Science and Engineering, Henan Polytechnic University, Jiaozuo 454003, China*
[5]*Institute of Flexible Electronics (IFE), Northwestern Polytechnical University (NPU), Xi'an 710072, China*

Correspondence should be addressed to Gengzhi Sun; iamgzsun@njtech.edu.cn and Wei Huang; iamwhuang@njtech.edu.cn

Received 28 October 2020; Accepted 27 January 2021; Published 2 March 2021

Copyright © 2021 Henghan Dai et al. Exclusive Licensee Science and Technology Review Publishing House. Distributed under a Creative Commons Attribution License (CC BY 4.0).

Lithium-sulfur (Li-S) batteries as power supply systems possessing a theoretical energy density of as high as 2600 Wh kg^{-1} are considered promising alternatives toward the currently used lithium-ion batteries (LIBs). However, the insulation characteristic and huge volume change of sulfur, the generation of dissolvable lithium polysulfides (LiPSs) during charge/discharge, and the uncontrollable dendrite formation of Li metal anodes render Li-S batteries serious cycling issues with rapid capacity decay. To address these challenges, extensive efforts are devoted to designing cathode/anode hosts and/or modifying separators by incorporating functional materials with the features of improved conductivity, lithiophilic, physical/chemical capture ability toward LiPSs, and/or efficient catalytic conversion of LiPSs. Among all candidates, molybdenum-based (Mo-based) materials are highly preferred for their tunable crystal structure, adjustable composition, variable valence of Mo centers, and strong interactions with soluble LiPSs. Herein, the latest advances in design and application of Mo-based materials for Li-S batteries are comprehensively reviewed, covering molybdenum oxides, molybdenum dichalcogenides, molybdenum nitrides, molybdenum carbides, molybdenum phosphides, and molybdenum metal. In the end, the existing challenges in this research field are elaborately discussed.

1. Introduction

The rapid development in materials science and technology has boomed the energy storage market, covering widespread applications of smart grids, electric vehicles, portable electronics, etc. [1–8]. Among all currently available battery systems, Li-S rechargeable batteries have drawn great attention because of their cost-effectiveness and extremely high energy density with a theoretical value of 2600 Wh kg^{-1}, which is much higher than that of the most advanced LIBs [9–16] and can meet the customers' requirements on electric vehicles with 500 kilometers (corresponding to 500–600 W h kg_{sul}^{-1}) per charge (Figure 1(a)) [17].

To date, the widely accepted reaction mechanism in Li-S batteries is the multielectron transfer mode ($S_8 + 16Li^+ + 16e^- \rightarrow 8Li_2S$), involving series reactions of $S_8 \rightarrow Li_2S_8 \rightarrow Li_2S_6/Li_2S_4 \rightarrow Li_2S_2/Li_2S$ accompanied by a number of intermediates generated during the charge/discharge process (Figure 1(b)) [18]. Since Li_2S (1.67 g cm^{-3}) has a lower density in comparison with sulfur (2.36 g cm^{-3}), there involves a volume expansion of ~80% during lithiation, thereby causing electrode degradation/pulverization [17]. Moreover, the insulation features of sulfur and Li_2S_2/Li_2S further hinder the electron transfer and slow down the reaction kinetics [19, 20]. In contrast to Li_2S_2 and Li_2S, the dissolvable lithium polysulfides (LiPSs) diffuse through the porous separator to the negative electrode and react with Li metal forming non-dissolvable Li_2S [21]. Such a "shuttle effect" results in the consumption of sulfur cathodes and the passivation of metal anodes, leading to the increase in internal resistance, the degradation of cycling stability, and the depression of Coulombic efficiency [22–25]. Meanwhile, the Li metal anode also suffers

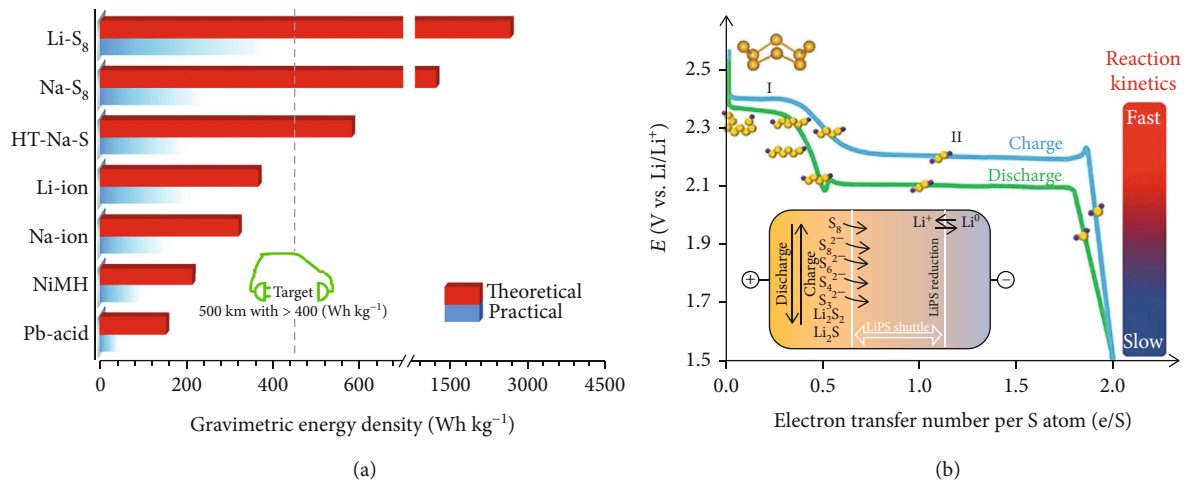


FIGURE 1: (a) The theoretical and practical gravimetric energy densities of different rechargeable batteries. Reproduced with permission from the Royal Society of Chemistry [17]. (b) The sulfur-based species produced during the charge/discharge process. Inset: the shuttle mechanism of LiPSs. Reproduced with permission from the Royal Society of Chemistry [18].

from high chemical reactivity, unstable solid electrolyte interphase (SEI), and dendrite growth during the plating/stripping process, resulting in capacity loss and safety issues [26]. These issues hamper the commercialization of Li-S batteries.

Numerous strategies have been raised to solve the above-mentioned problems, such as designing cathode/anode hosts and/or modifying separators [27]. Early tries focused on the incorporation of sulfur into carbonaceous materials, such as graphene foam [28], porous carbon [29], and carbon nanotube network [30], which provide physical constraints on LiPSs. However, the weak intermolecular interaction between nonpolar hydrophobic carbonaceous hosts and polar hydrophobic LiPSs is insufficient to prevent the shuttle of LiPSs. Alternatively, polar substances, e.g., transition metal oxides [31], sulfides [32], and carbides [33], were proposed to enhance the adsorption of LiPSs; nevertheless, the performance improvement remains moderate. Lately, the strategies based on the acceleration of the conversion between LiPSs and Li_2S_2/Li_2S were developed and a number of nanomaterials (e.g., oxides [34], sulfides [35], selenides [36], nitrides [37], carbides, phosphides [38], and metal [39]) have been proven to exhibit catalytic properties. Other viable approaches include the modification of separators to realize the limitation of LiPSs on the cathode side, thereby weakening the shuttle effect, and the protection of Li metal anodes [21]. In general, the overall principle is to incorporate functional materials with the features of improved conductivity, physical/chemical capture ability toward LiPSs, and/or efficient catalytic conversion of LiPSs so as to enhance the device performance.

Molybdenum-based (Mo-based) materials are highly preferred due to their tunable crystal structure, adjustable composition, and variable valence of Mo centers, enabling their strong interaction with the soluble LiPSs via a variety of mechanisms for inhibiting the "shuttle effect," such as polar-polar adsorption, Lewis acid-base interaction, and conversion reaction. Moreover, some Mo-based materials are also reported lithiophilic, which is helpful to suppressing

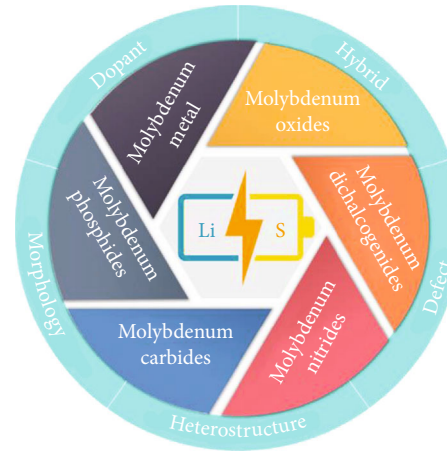


FIGURE 2: The classification and material design strategies of Mo-based materials for Li-S batteries.

the formation of Li dendrites on anodes and prolonging the cycle life of Li-S batteries [40–42]. Herein, for the first time, we comprehensively review the design and application of Mo-based materials in Li-S batteries (Figure 2), elaborately reveal the interaction between Mo-based materials and LiPSs, and critically discuss the basic mechanism in enhancing adsorption and reaction kinetics. Finally, we summarize the challenges and outline the future prospects of using Mo-based materials in Li-S batteries.

2. Molybdenum Oxides

Molybdenum oxides possess a variable valence and adjustable bandgap, which have been widely applied in electronics [43], catalysis [44], energy storage [45], and electrochromic devices [46]. Their crystal and electronic structures can be facilely manipulated through morphology control, defect engineering (e.g., oxygen vacancy and dopants), and composition adjustment. Particularly, in this section, MoO_3 and

MoO_2 are introduced by discussing their intrinsic properties, modification strategies, and critical roles in Li-S batteries.

2.1. MoO_3. MoO_3 (orthorhombic phase, α-MoO_3) possesses a layered structure composed of thin sheets with a thickness of ~0.7 nm which contains linked and distorted MoO_6 octahedra [40]. The bandgap of α-MoO_3 is >2.7 eV, and the electrical conductivity was reported to be ~10^{-5} S cm^{-1} [49]. When used as a cathode matrix, the metal-oxygen bond enables α-MoO_3 strong polarity toward efficient LiPS trapping [50]. In this regard, Yi et al. hydrothermally synthesized MoO_3 nanobelts with a width of ~200 nm and a length of ~1.5 μm, then used them as a cathode matrix for sulfur loading (Figures 3(a)–3(d)) [47]. Based on experimental results and DFT (density functional theory) calculations, they found that oxygen defects (ODs) not only improve the electrical conductivity of MoO_3 but also obviously enhance the binding strength between MoO_3 and Li_2S_6, effectively anchoring LiPS intermediates during cycling. In addition, both MoO_3 and MoO_{3-x} exhibited catalytic properties toward the reversible conversion of LiPSs tested in symmetric cells using Li_2S_6 solution as the electrolyte. Comparably, MoO_{3-x} showed higher activity with a large current and distinct redox peaks than MoO_3, manifesting an enhanced conversion of LiPSs. Compared to MoO_3/S (1060 mAh g^{-1} at 0.2 C), MoO_{3-x}/S cathodes delivered a similar capacity of 1076 mAh g^{-1} under 0.2 C with superior cycling stability, retaining 690 mAh g^{-1} after 200 cycles.

In addition to oxygen defects, the intrinsic properties of MoO_3 can also be adjusted by inserting guest atoms or molecules into their van der Waals interlayer gaps [51]. Following this direction, Yang et al. prepared tin- (Sn-) intercalated MoO_3 ($Sn_{0.063}MoO_3$) via the disproportionation of Sn(II) (Figures 3(e)–3(g)) [48]. DFT calculations indicated that the electron transferred from the intercalated Sn atoms to MoO_3 resulted in the emergence of the spreading states around the Fermi level. This led to enhanced electrical conductivity and binding energies of Li_2S_4 and S_8 to $Sn_{0.063}MoO_3$, which therefore effectively improved the cathode rate performance and depressed the LiPS shuttle. The as-fabricated Li-S battery delivered an initial capacity of 906 mAh g^{-1} at 1 C with 79.6% retention after 500 cycles.

Hybridizing with carbonaceous materials is another viable way to mitigate the low electrical conductivity of MoO_3. A typical work was presented by Chen et al., where a freestanding membrane containing a cathode layer of MoO_3/CNT/S (FMC/S) and a LiPS-blocking layer of intertwined MoO_3/CNTs was fabricated via a sequential filtration method (Figure 4) [52]. In this manner, the interfacial binding strength between the two layers was improved, and the poor conductivities of sulfur and MoO_3 were effectively alleviated. Combined with the strong polarity of α-MoO_3, LiPSs were effectively trapped. The device delivered a specific capacity of 1074 mAh g^{-1} at 0.5 C, retaining 666 mAh g^{-1} after 350 cycles.

In addition to designing a cathode matrix, the idea of modifying separators was adopted to relieve the shuttle effect of LiPSs, which is comparably a low-cost strategy [56]. Imtiaz et al. coated MoO_3-based slurry onto the commercial separator forming a porous network (Figures 5(a)–5(c)) [53]. Such a hybrid separator in Li-S batteries enabled fast ion transportation. Due to the catalytic property of MoO_3 and the intimate contact between the cathode and the separator, the as-assembled symmetric cell provided increased current density and sharper redox peaks compared to that based on the routine separator and CNT-modified separator. The as-fabricated Li-S battery exhibited a specific capacity of 1377 mAh g^{-1} at 0.5 C with retention of 49.7% after 200 cycles. Following this idea, Kaisar et al. further designed a modified polypropylene separator with lithium-passivated MoO_3 nanobelts [57]. The as-prepared battery achieved an improved capacity at 0.5 C (717 mAh g^{-1} after 500 cycles), attributable to (i) the strong adsorption of MoO_3 to LiPSs and (ii) the increased conductivity of MoO_3 owing to the lithiation (Li_xMoO_3) [58]. Further enhancement in the adsorption ability of MoO_3 can be achieved by hybridizing with carbonaceous materials. The interwoven MoO_3@CNT-modified separator fabricated via the vacuum filtration method by Luo et al. not only provided abundant charge (electrons and ions) transport pathways but also effectively mitigated the LiPS shuttle (Figures 5(d) and 5(e)) [54]. The resultant Li-S cell showed a specific capacity of 1070 mAh g^{-1} at 0.3 C with 61.2% retained at 3 C (655 mAh g^{-1}). Moreover, when cycling at 1 C for 400 cycles, the device maintained 53.4% of the initial capacity, corresponding to 641 mAh g^{-1}.

Since Li metal has high activity, the presence of LiPSs leads to the generation of insulating Li_2S_2/Li_2S on the Li surface, promoting the formation of Li dendrites and shortening the anode lifespan. Therefore, in addition to the enhancement of cathode performance, the effective inhibition of LiPS shuttling also protects Li metal anodes from the corrosion by LiPSs. In a recent work shown in Figures 5(f) and 5(g), a freestanding MoO_3/carbon nanofiber (MoO_3/CNF) membrane was prepared by solvothermally depositing MoO_3 nanoparticles on the carbonized electrospun PAN nanofibers and used as an interlayer in Li-S batteries [55]. The combination of the polar MoO_3 and conductive CNF network efficiently facilitates the conversion between Li_2S_2/Li_2S and sulfur species, suppressing LiPS shuttling. The symmetric battery (Li|Li) with the MoO_3/CNF interlayer exhibited improved cycling stability over 400 h of testing at 0.5 mA cm^{-2} under 1 mAh cm^{-2} and smaller overpotential than the devices made of the CNF interlayer and pristine separator (Figure 5(g)).

2.2. MoO_2. Different from MoO_3, monoclinic MoO_2 has a deformed rutile structure with a tetragonal orientation, where the MoO_6 octahedra share the opposite edges along the crystallographic *c*-axis [40]. Typically, it displays higher electrical conductivity compared with MoO_3, due to the small bandgap [61]. Wu et al. grew MoO_2 hollow spheres on N-doped graphene (MoO_2/G) via hydrothermal reaction and used them as the sulfur host (Figures 6(a)–6(c)) [59]. In comparison with the physical mixture of MoO_2 and graphene, MoO_2/G exhibited enhanced rate performance and stability attributable to the enlarged accessible surface of N-doped graphene, the strong interaction between LiPSs and MoO_2, and the efficient electron transfer between N-doped

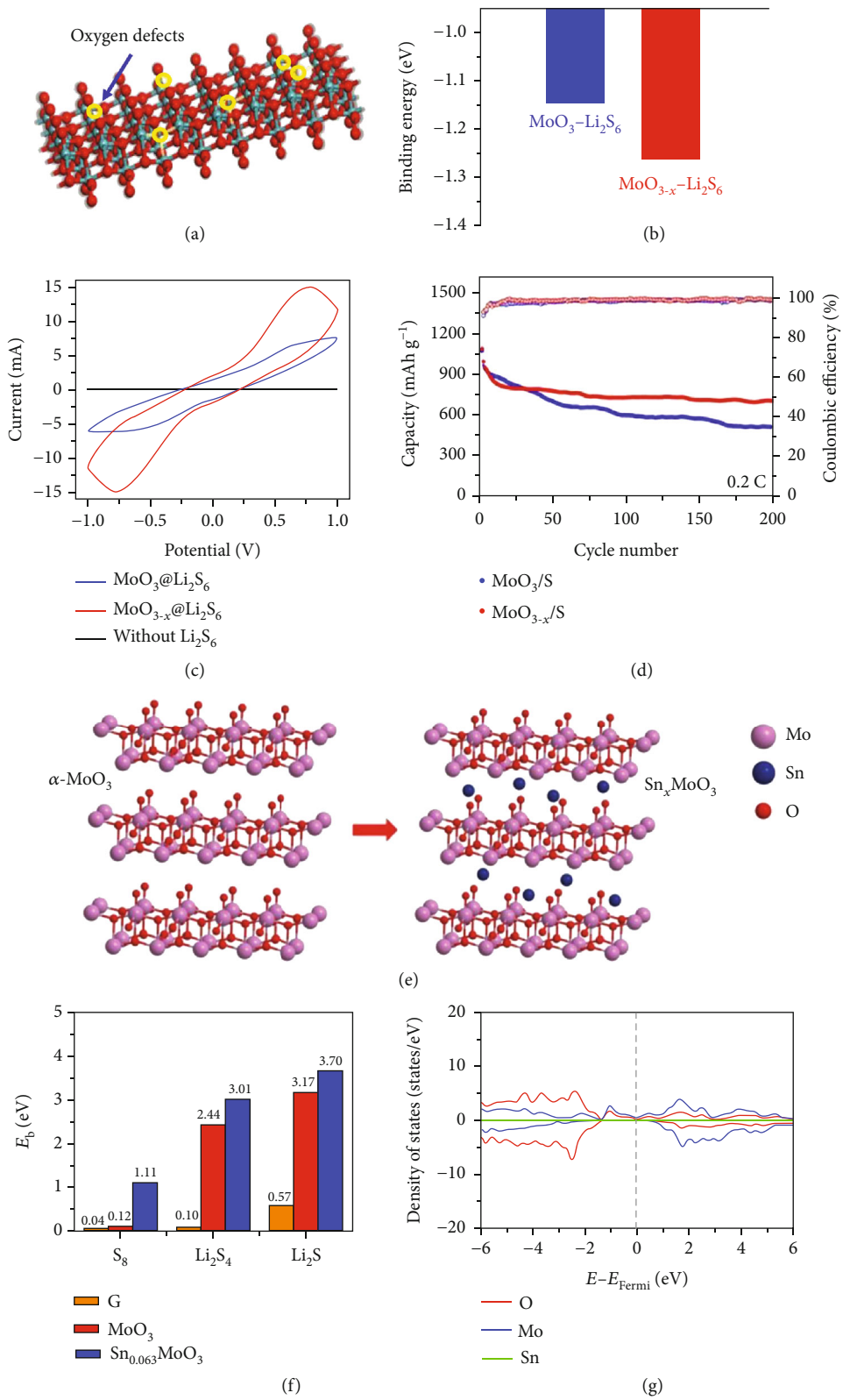


FIGURE 3: (a) Schematic illustration of the oxygen defects (ODs) on MoO_{3-x}. (b) The calculated binding energies of Li_2S_6 with MoO_3 and MoO_{3-x}, respectively. (c) Cyclic voltammetry (CV) curves of symmetric cells based on MoO_3 and MoO_{3-x} electrodes with and without Li_2S_6. (d) Cycling performances of MoO_3/S and MoO_{3-x}/S cathodes at 0.2 C. (a–d) Reproduced with permission from Wiley-VCH [47]. (e) Schematic illustration showing the intercalation of tin (Sn) atoms into MoO_3. (f) Calculated binding strength for S_8, Li_2S_4, and Li_2S on graphene, MoO_3, and Sn-intercalated MoO_3 ($Sn_{0.063}MoO_3$), respectively. (g) Density of states (DOS) for $Sn_{0.063}MoO_3$. (e–g) Reproduced with permission from Wiley-VCH [48].

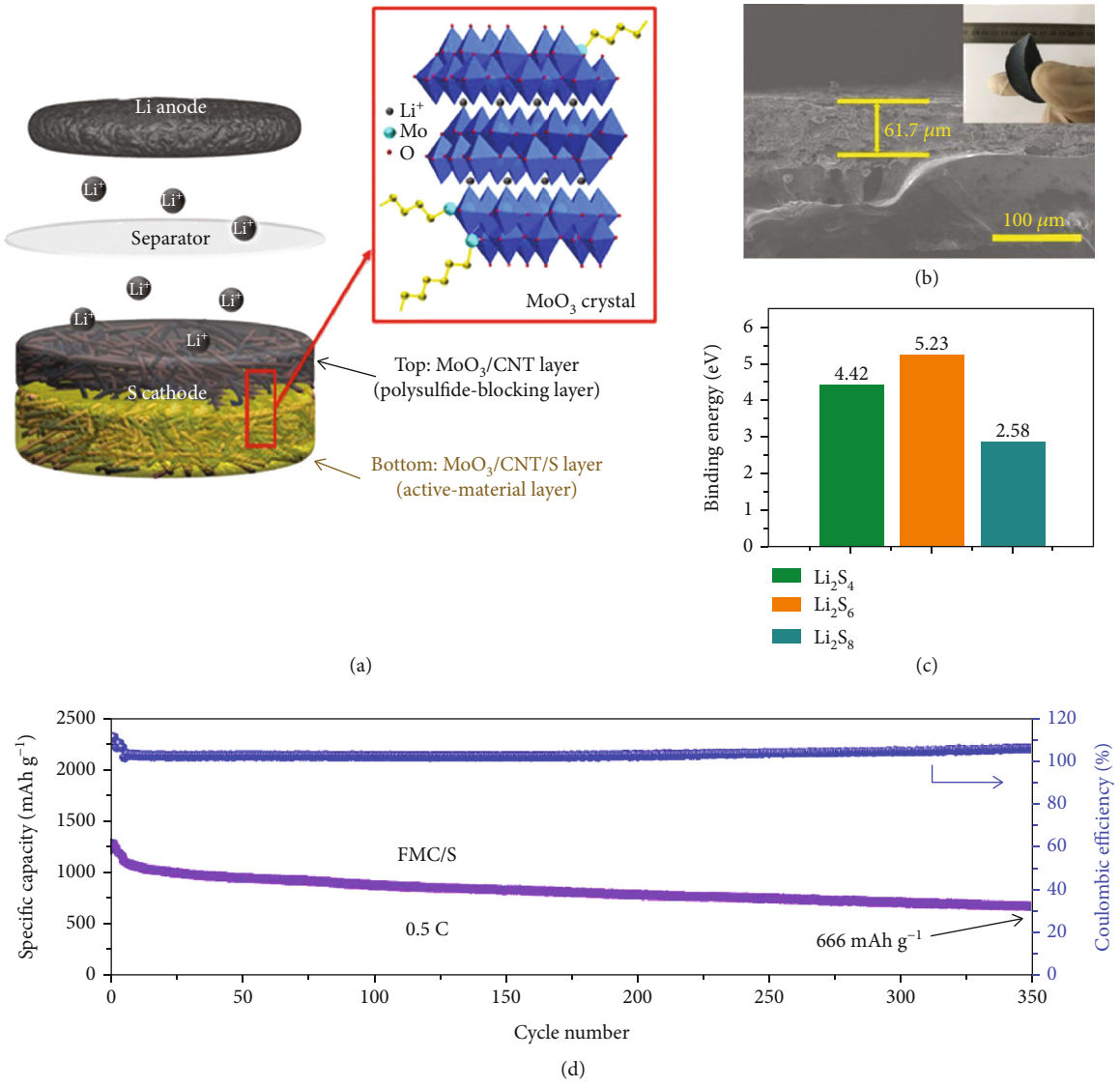


FIGURE 4: (a) Li-S battery adopting freestanding MoO_3/CNT/S (FMC/S) as the cathode. (b) Cross-sectional observation of the FMC/S membrane. Inset: bending test of the FMC/S membrane. (c) The calculated binding energies between MoO_3 and LiPSs (including Li_2S_4, Li_2S_6, and Li_2S_8). (d) Cycling stability of the FMC/S at 0.5 C. (a–d) Reproduced with permission from the American Chemical Society [52].

graphene and MoO_2 via the C-O-Mo bond. MoO_2/G/S delivered specific capacities of 810 mAh g^{-1} at 1 C and maintained 664 mAh g^{-1} after 500 cycles.

Porous structure was proposed to alleviate the volume expansion of sulfur during lithiation and in the meantime restrict the LiPS shuttle. Wang et al. prepared porous frameworks composed of MoO_2 and carbon (MoO_2/C-NC) through the carbonization of Cu-Mo-MOF (metal-organic frameworks) followed by $FeCl_3$ etching (Figures 6(d)–6(f)) [60]. Sulfur was homogeneously distributed in porous MoO_2/C-NC. In comparison with the bare carbonaceous host, MoO_2/C-NC exhibited high electrical conductivity and strong interactions to LiPSs via Li-O and Mo-S bonds. As a result, the MoO_2/C-NC-based symmetrical cells presented improved reaction kinetics with higher current density and lowered overpotential with minimized potential separation between redox peaks, confirming that MoO_2 accelerated the electrochemical reactions of LiPSs. At 0.5 C, the MoO_2/C-NC/S electrode delivered 801 mAh g^{-1} after 200 cycles, corresponding to 73.4% retention of the initial capacity. Following this direction, Razaq et al. prepared the MoO_2/rGO host by annealing Mo-based MOF (Mo-MOF) wrapped with graphene oxide (GO) in Ar [62]. The obtained MoO_2 microrods featured crispy rice-like mesoporous structure and exhibited high electron and Li^+ conductivity, good confinement for LiPSs, and catalytic conversion of LiPSs to thiosulfates (polythionates). Consequently, the MoO_2/rGO/S cathode showed good charge/discharge stability at 0.5 C for 500 cycles with a capacity of 1027 mAh g^{-1}, corresponding to 90.0% retention of the initial value.

The interlayer based on the combination of MoO_2 and carbon materials was inserted between the sulfur cathode and the separator [64]. Zhuang et al. incorporated MoO_2 nanoparticles into carbon nanofibers by carbonizing the

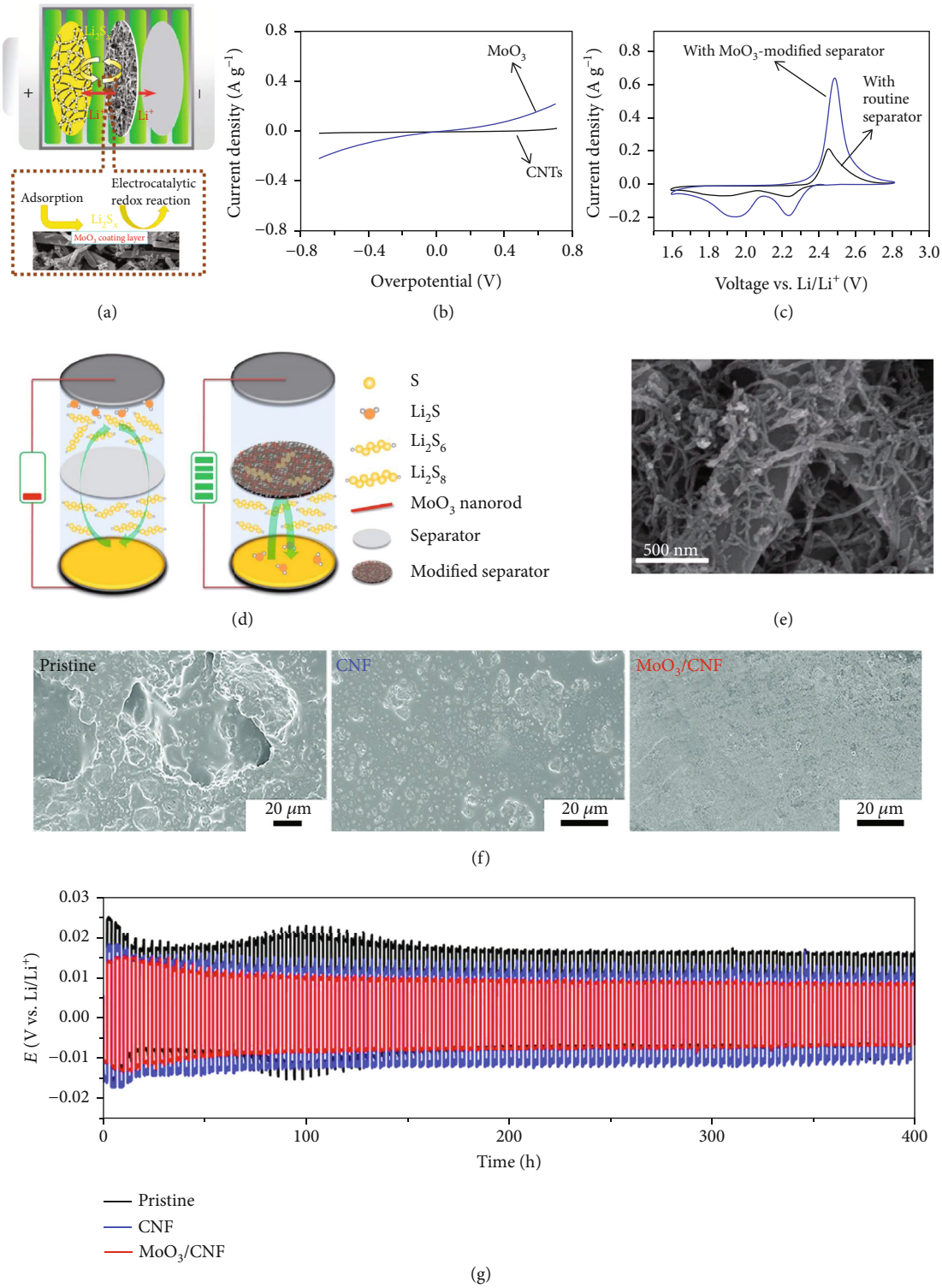


Figure 5: (a) Li-S battery based on the CNT/S cathode together with a separator modified by MoO_3. (b) Polarization curves of Li-S cells containing Li_2S_6 in a symmetric configuration. (c) CV behaviors of the Li-S battery containing the MoO_3-modified separator in comparison with that based on the routine separator. (a–c) Reproduced with permission from Wiley-VCH [53]. (d) Li-S batteries based on pristine and modified (MoO_3@CNT) separators. (e) SEM image of the MoO_3@CNT network. (d, e) Reproduced with permission from the Royal Society of Chemistry [54]. (f) The surface morphology of Li metal anodes with pristine, CNF-modified, and MoO_3/CNF-modified separators after cycling at 1 C for 500 times. (g) Voltage-time profiles of the symmetric batteries (Li|Li) with pristine, CNF-modified, and MoO_3/CNF-modified separators (testing conditions: 0.5 mA cm^{-2} and 1 mAh cm^{-2}). (f, g) Reproduced with permission from the Royal Society of Chemistry [55].

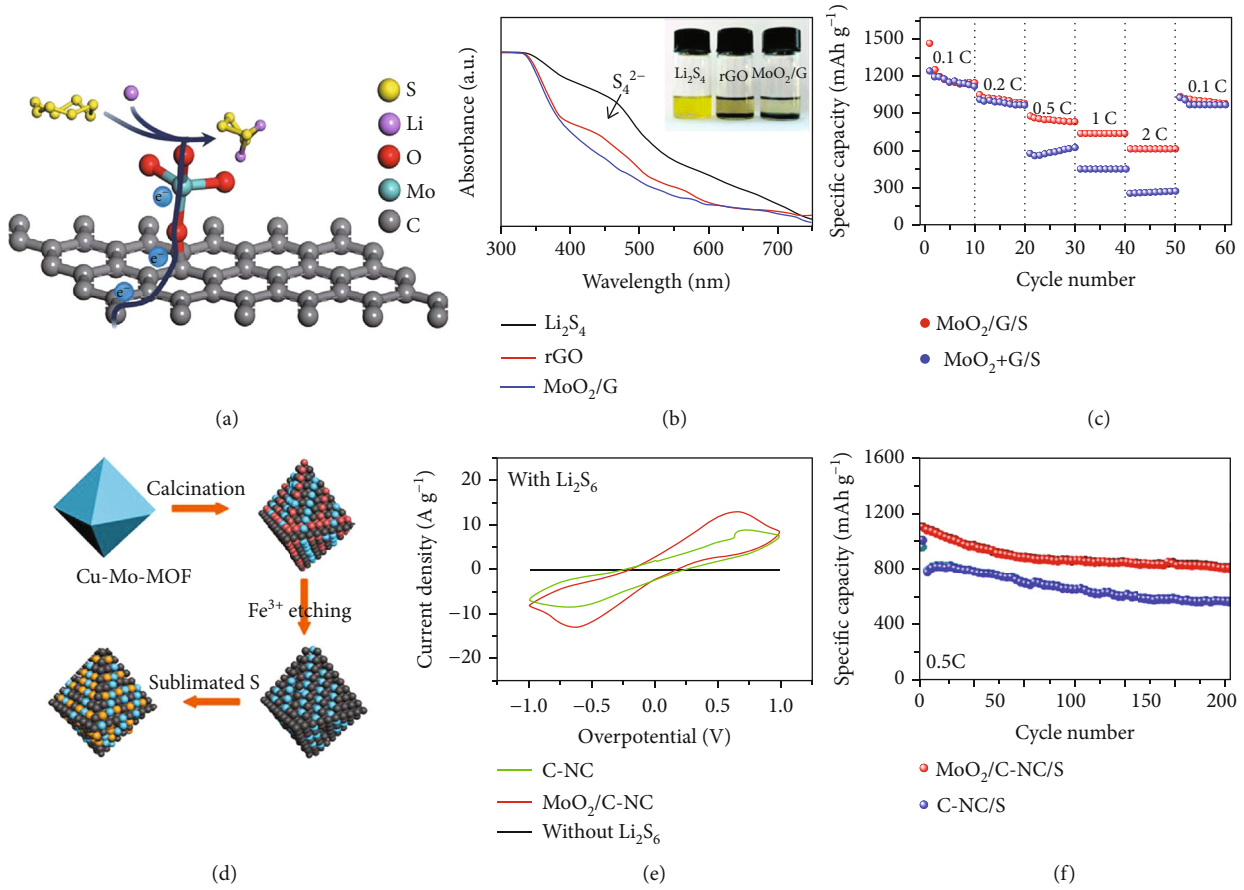


FIGURE 6: (a) The charge transfer between MoO_2/G and LiPSs. (b) The adsorption capabilities of MoO_2/G and graphene to Li_2S_4 evidenced by UV-vis spectra. (c) The rate performance of MoO_2/G/S cathodes compared to that of MoO_2+G/S. (a–c) Reproduced with permission from the Royal Society of Chemistry [59]. (d) The synthesis of MoO_2/C-NC/S. (e) CV curves of the symmetrical Li_2S_6 cells. (f) The stability of MoO_2/C-NC/S and C-NC/S cathodes at 0.5 C. (d–f) Reproduced with permission from the American Chemical Society [60].

electrospun membrane that consisted of PAN fibers and phosphomolybdic acid (PMA: $H_3PO_4{\cdot}12MoO_3$) (Figure 7) [63]. The obtained MoO_2-CNF interlayer can effectively trap LiPSs and improve the reversibility of sulfur reaction during charge/discharge. The as-fabricated battery with the MoO_2-CNF interlayer showed capacity retention of 73.0% at 0.4 mA cm^{-2} after 150 cycles, corresponding to 1006 mAh g^{-1}.

Molybdenum oxides have strong polarity with Lewis acid sites (Mo) and Lewis base sites (O) for capturing LiPSs and the subsequent catalytic conversion. However, they typically have low conductivity and small specific surface areas [23], which are not conducive to the electron transfer and LiPS adsorption/conversion during cycling. Therefore, in order to improve their performance in Li-S batteries, defect engineering (e.g., oxygen vacancies), intercalation (e.g., Sn), hybridization with conductive filaments (e.g., CNT and rGO), and structure design (e.g., hollow cages and porous frameworks) are highly necessitated.

3. Molybdenum Dichalcogenides

During the past decade, the 2D molybdenum dichalcogenides (e.g., MoS_2 and $MoSe_2$) have drawn great attention due to their unique features of tunable compositions, crystal structures, valence states, and morphologies, endowing them with high electrochemical activities and potential applications in energy storage [35, 36, 65–68]. In this section, recent advances in these two kinds of molybdenum dichalcogenides are discussed.

3.1. MoS_2. Single-layer molybdenum disulfide (MoS_2) is composed of Mo (+4) and S (−2) atoms arranged into a sandwiched structure via covalent bonds of S-Mo-S, whereas MoS_2 nanosheets are held together through relatively weak interaction of van der Waals forces [73]. Due to the unsaturated bonding at the defect sites (e.g., edge and vacancies), MoS_2 facilitates the catalytic conversion of LiPSs [74–76]. Babu et al. synthesized MoS_2 nanoflakes by chemical vapor deposition (CVD) and cycled them against lithium foil in a cell containing $LiNO_3$, LiTFSI, and Li_2S_4 as the catholyte [69]. The experimental observation showed the unsaturated sulfur sites on the edge of MoS_2 facilitated the adsorption and subsequent catalytic conversion of LiPSs to Li_2S_2/Li_2S (Figures 8(a) and 8(b)).

Recently, the combination of metal sulfides and oxides has been confirmed to offer improved adsorption ability toward LiPSs. In a typical work, Wang et al. grew

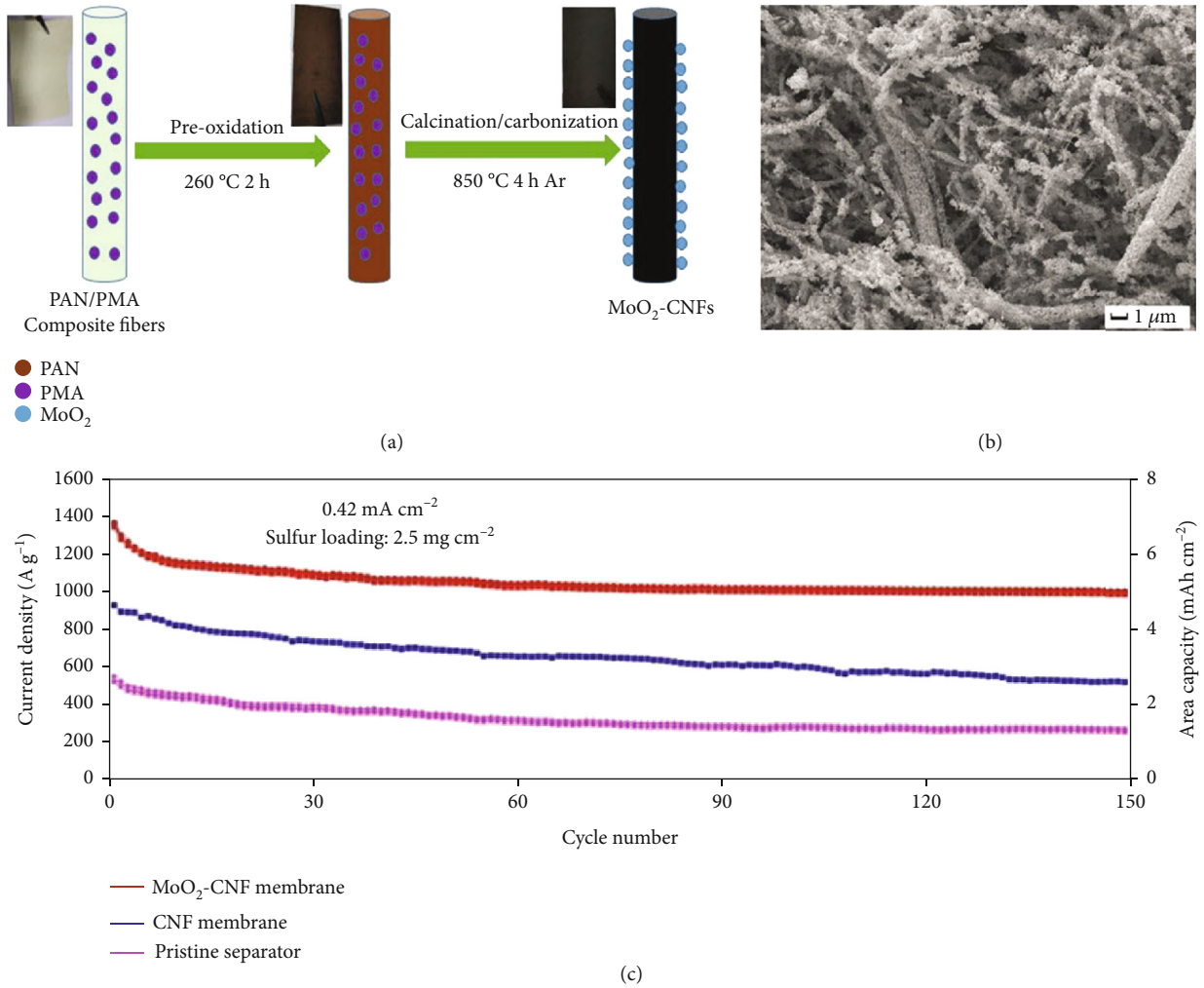


FIGURE 7: (a) Formation process of MoO_2-CNF. (b) SEM image of MoO_2-CNF. (c) Cycling stabilities of the Li-S battery without the interlayer and the devices with interlayers of CNF and MoO_2-CNF, respectively. (a–c) Reproduced with permission from Wiley-VCH [63].

C@SnO_2/1T-MoS_2 (C@SnO_2/TMS) arrays with hierarchical architectures on carbon cloth via hydrothermal reaction and used them as the host for sulfur [70]. In this hierarchical structure, SnO_2 nanosheets that consisted of small nanoparticles were coated by 1T-MoS_2 (Figures 8(c) and 8(d)). On the one hand, the porous structure effectively suppressed the volume change of sulfur and in the meantime allowed fast transportation of Li^+ [77]. On the other hand, SnO_2 provided stronger adsorption to Li_2S_4 compared to MoS_2 (0.46 eV) with a binding energy of 2.64 eV according to DFT calculations, while 1T-MoS_2 nanosheets with high conductivity and abundant edges accelerated the redox kinetics of LiPSs effectively. The resultant C@SnO_2/TMS/S cathode delivered 710 mAh g^{-1} at 5 C with 63.0% retained after 4000 cycles.

The catalytic activity of MoS_2 can be further tuned via defect engineering. For instance, Lin et al. introduced sulfur vacancies in MoS_2 and evaluated its effect on the catalytic conversion of LiPSs (Figure 8(e)) [71]. In a typical synthesis, MoS_2 nanoflakes were prepared by liquid-phase exfoliation and mixed with GO by filtration. Such composites were thermally treated in hydrogen at 600°C for 6 h. The amount of sulfur deficiencies was varied by changing annealing duration and temperature. The catalytic behavior of MoS_{2-x} on the conversion of LiPSs was revealed in symmetric cells with 0.2 M Li_2S_6 as the electrolyte. The results indicated that the sulfur deficiencies in MoS_{2-x} rendered MoS_{2-x}/rGO more active sites and facilitated the redox conversion of sulfur to LiPSs. The sulfur cathode with 4.0 wt% of MoS_{2-x}/rGO showed specific capacities of 1159 mAh g^{-1} and 827 mAh g^{-1} at 0.5 C and 8 C, respectively. Liu et al. incorporated defect-rich MoS_2 into porous graphene aerogel (denoted as GA-DR-MoS_2) and further confirmed that abundant defects assisted efficient adsorption and catalytic reactions of LiPSs during electrochemical cycling [78]. The resultant GA-DR-MoS_2-based cathode containing 70.0 wt% of sulfur presented a discharging capacity of 581 mAh g^{-1} under 5 C.

In another work, Lin et al. decorated moss-like $Mo_{0.9}Co_{0.1}S_2$ nanosheets on the CNT surface by the hydrothermal method forming a core-shell tubular structure followed by phosphorus doping (P doping) at elevated temperature using red phosphorus as the precursor (Figure 8(f)) [72]. The experimental results demonstrated that MoS_2 nanotubes codoped by Co and P atoms improved the catalytic conversion of LiPSs in both directions (the sulfur reduction and

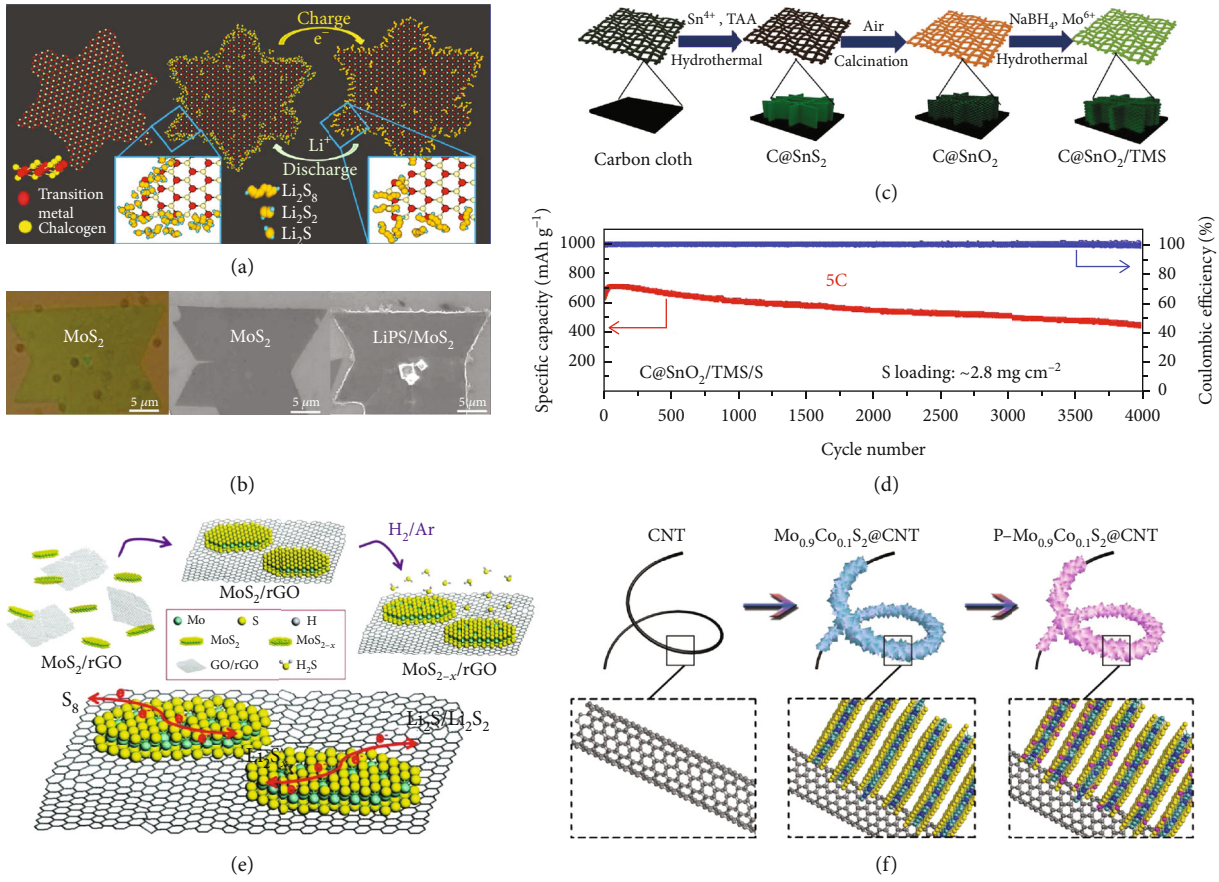


FIGURE 8: (a) Schematic illustration for the confined deposition and conversion of LiPSs at the preferential catalytic sites of transition metal dichalcogenide (TMD) nanosheets. (b) Optical and SEM images of MoS_2 flakes and LiPS-deposited MoS_2 flakes at the discharged state. (a, b) Reproduced with permission from the American Chemical Society [69]. (c) The synthesis of the hierarchical C@SnO_2/TMS nanoarray on carbon cloth. (d) Long-term cycling stability test of the C@SnO_2/TMS/S cathode at 5 C. (c, d) Reproduced with permission from the American Chemical Society [70]. (e) The synthesis of MoS_{2-x}/rGO and the conversion of Li_2S_x. Reproduced with permission from the Royal Society of Chemistry [71]. (f) The synthesis of cobalt (Co) and phosphorus (P) codoped MoS_2 (P-$Mo_{0.9}Co_{0.1}S_2$) on CNT. Reproduced with permission from Wiley-VCH [72].

the sulfur evolution). Particularly, Co doping induced the formation of 1T-MoS_2, guaranteeing low electron transport resistance, while P dopants provided an electron-rich environment in the $Mo_{0.9}Co_{0.1}S_2$, which was conducive to the scission of the S-S bonds. Consequently, the P-$Mo_{0.9}Co_{0.1}S_2$/S showed 1187 mAh g^{-1} at 0.5 C after 150 cycles, corresponding to 89.0% retention of the initial capacity.

Similar to molybdenum oxides, MoS_2 was also used to modify the separator as a barrier to alleviate the LiPS shuttle effect. As a typical example, Ghazi et al. exfoliated MoS_2 nanosheets via Li^+ intercalation and filtrated them on commercial Celgard separators (MoS_2/Celgard) for Li-S batteries (Figures 9(a)–9(c)) [79]. Electrochemical impedance spectroscopy (EIS) disclosed that MoS_2/Celgard showed rapid Li^+ diffusion with similar conductivity (2.0×10^{-1} mS cm^{-1}) to bare Celgard (3.3×10^{-1} mS cm^{-1}) but much higher than GO/Celgard (3.1×10^{-2} mS cm^{-1}). The reason was assigned to the high Li^+ density on the MoS_2 surfaces generated during exfoliation. In addition, the MoS_2/Celgard separator also effectively blocked LiPSs due to the presence of MoS_2. The battery with the MoS_2/Celgard separator exhibited 808 mAh g^{-1} at 0.5 C initially and retained 401 mAh g^{-1} after 600 cycles. Zheng et al. modified the Celgard separator by edge-rich MoS_2/C hollow microspheres (Edg-MoS_2/C HMs) by hydrothermal reaction [81]. The Edg-MoS_2/C HMs enabled the efficient conversion of LiPSs and provided abundant sites for Li_2S absorption. The as-fabricated cells with sulfur loading of 1.7 mg cm^{-2} and 6.1 mg cm^{-2} delivered capacities of 896 mAh g^{-1} and 554 mAh g^{-1} at 0.5 C, respectively. Wu et al. designed a separator with dual functionality via a layer-by-layer self-assembly strategy (Figures 9(d) and 9(e)) [80]. The positively charged MoS_2-poly(diallyl dimethyl ammonium chloride) (PDDA) (denoted as M-P) hybrid and the negatively charged poly(acrylic acid) (PAA) were alternatively deposited on the commercial separator (denoted as M-P/P) forming a "nanobrick wall" structure. The PAA mortars selectively impeded the travel of large LiPSs (1–2 nm) compared to Li^+ because of their strong binding energies toward Li_2S_2, Li_2S_4, and Li_2S_6, while well-orientated MoS_2 nanosheet bricks catalyzed the conversion of LiPSs to the insoluble thiosulfate and polythionate complex, which further anchored LiPSs from solution and ultimately converted to Li_2S_2/Li_2S. As a result, the separator with 0.1 mg cm^{-2} of M-P/P coating endowed the Li-S battery 423 mAh g^{-1}

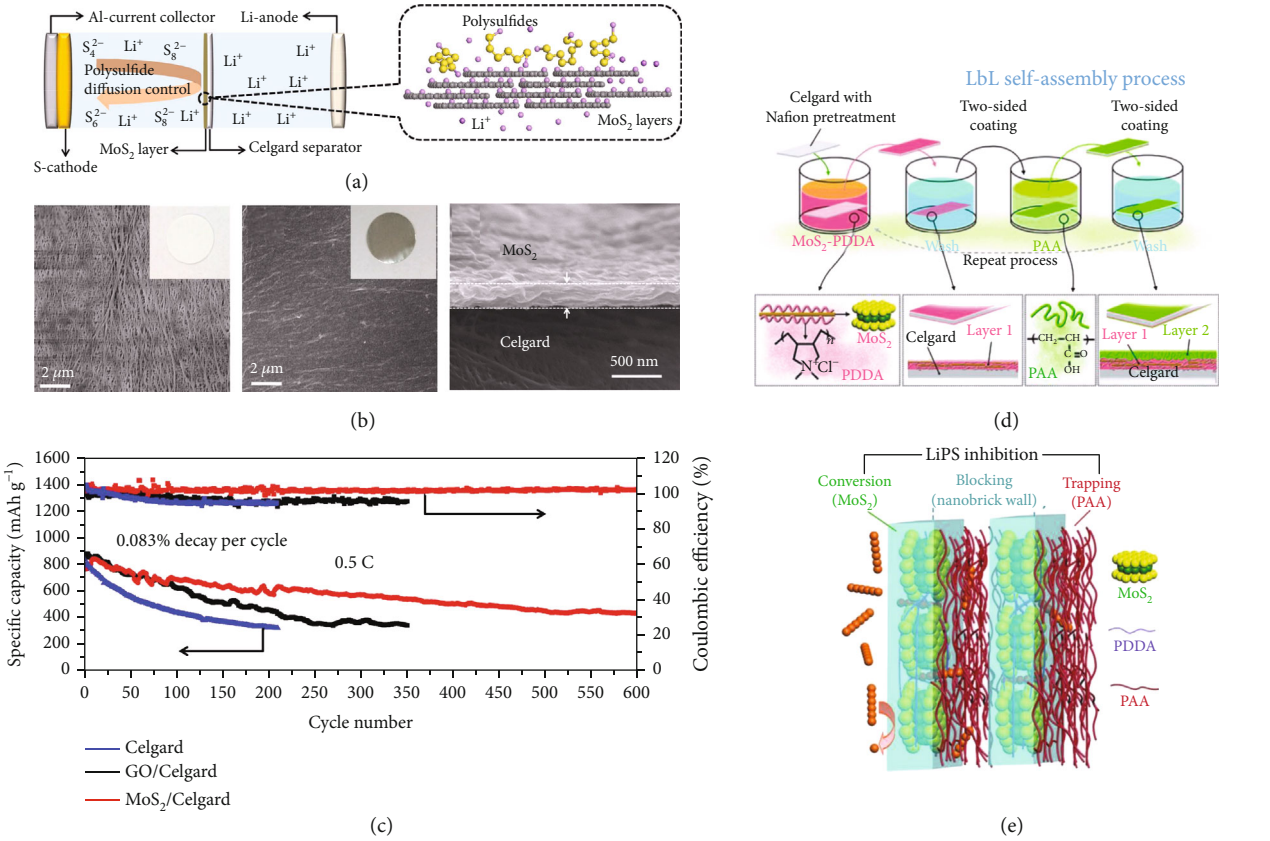


FIGURE 9: (a) Li-S battery based on the MoS_2/Celgard separator. (b) SEM images of the Celgard surface (inset: the photograph of pristine Celgard), MoS_2/Celgard surface (inset: the photograph of MoS_2-coated Celgard), and cross-section of MoS_2 layers. (c) Long-term cycling tests of Li-S cells constructed by MoS_2/Celgard, GO/Celgard, and Celgard separators. (a–c) Reproduced with permission from Wiley-VCH [79]. (d) The preparation of the MoS_2-PAA-modified separator assembled in a layer-by-layer manner. (e) The trapping and conversion of LiPSs on the MoS_2-PAA-modified separator. (d, e) Reproduced with permission from Wiley-VCH [80].

after 2000 cycles at 1 C, corresponding to 42.0% retention of the initial capacity.

In 2018, Cha and coworkers made the first attempt to protect Li metal anodes by sputtering a thin layer of 2H MoS_2 with a thickness of ~10 nm (Figure 10(a)) [82]. The subsequent lithiation transformed the crystal phase of MoS_2 from semiconducting 2H to metallic 1T (Figure 10(b)), thereby lowering the interfacial impedance (between the Li metal and the electrolyte). Moreover, 1T-MoS_2 has a small Li migration energy barrier of 0.155 eV, which is beneficial for the rapid diffusion of Li^+ to Li metal and the homogeneous Li deposition. The modification of lithiated MoS_2 led to low-voltage polarization of ~52 mV at 10.0 mA cm^{-2}, a threefold improvement in the cycle life compared to bare Li metal, and effective suppression of Li dendrites (Figures 10(c) and 10(d)). The Li-S batteries made of the CNT-S cathode and MoS_2-modified Li anode exhibited a high capacity of 1105 mAh g^{-1} with excellent retention of 84.0% over 1200 cycles at 0.5 C (Figure 10(e)).

3.2. $MoSe_2$. Molybdenum diselenides ($MoSe_2$) have been applied in LIBs as anode materials since the 1970s because of their high capacity and long cycle life [36, 85, 86]. Similar to MoS_2, $MoSe_2$ also exhibit preferential adsorption of LiPSs at the edge sites due to the unsaturated bonding of Se [87]. Wong et al. synthesized the $MoSe_2$/N-rGO hybrid as the sulfur host for Li-S batteries. The triangular-shaped $MoSe_2$ with a lateral size of 10–60 nm were loaded on N-doped graphene by the CVD method (Figure 11(a)) [83]. Theoretical calculation (Figures 11(b) and 11(c)) indicated that $MoSe_2$ exhibited a lower Li diffusion energy barrier of 0.2374 eV compared with graphene (0.3104 eV). The obtained $MoSe_2$/N-rGO/S electrode delivered a capacity of 887 mAh g^{-1} after charged/discharged at 0.2 C for 100 cycles (Figure 11(d)), corresponding to 86.3% retention.

Tian et al. decorated $MoSe_2$ nanoflakes on rGO using hydrothermal reaction and employed linear sweep voltammetry (LSV) at the full discharge state and potentiostatic method to study the catalytic properties of $MoSe_2$ on the LiPS conversion in Li-S batteries (Figures 11(e)–11(g)) [84]. The experimental results showed that the presence of $MoSe_2$ facilitated the full conversion of LiPSs and nucleation of Li_2S. Consequently, the $MoSe_2$@rGO/S cathode retained 941 mAh g^{-1} (78.4% of the initial capacity) after charged/discharged for 200 cycles at 0.5 C.

Molybdenum dichalcogenides show site-selective catalytic performance and phase-dependent conductivity. Typically, defect sites (e.g., edge and vacancies) exhibit higher catalytic activity than basal planes, while the 1T phase has a lower energy barrier for both electron transport (facilitating catalytic

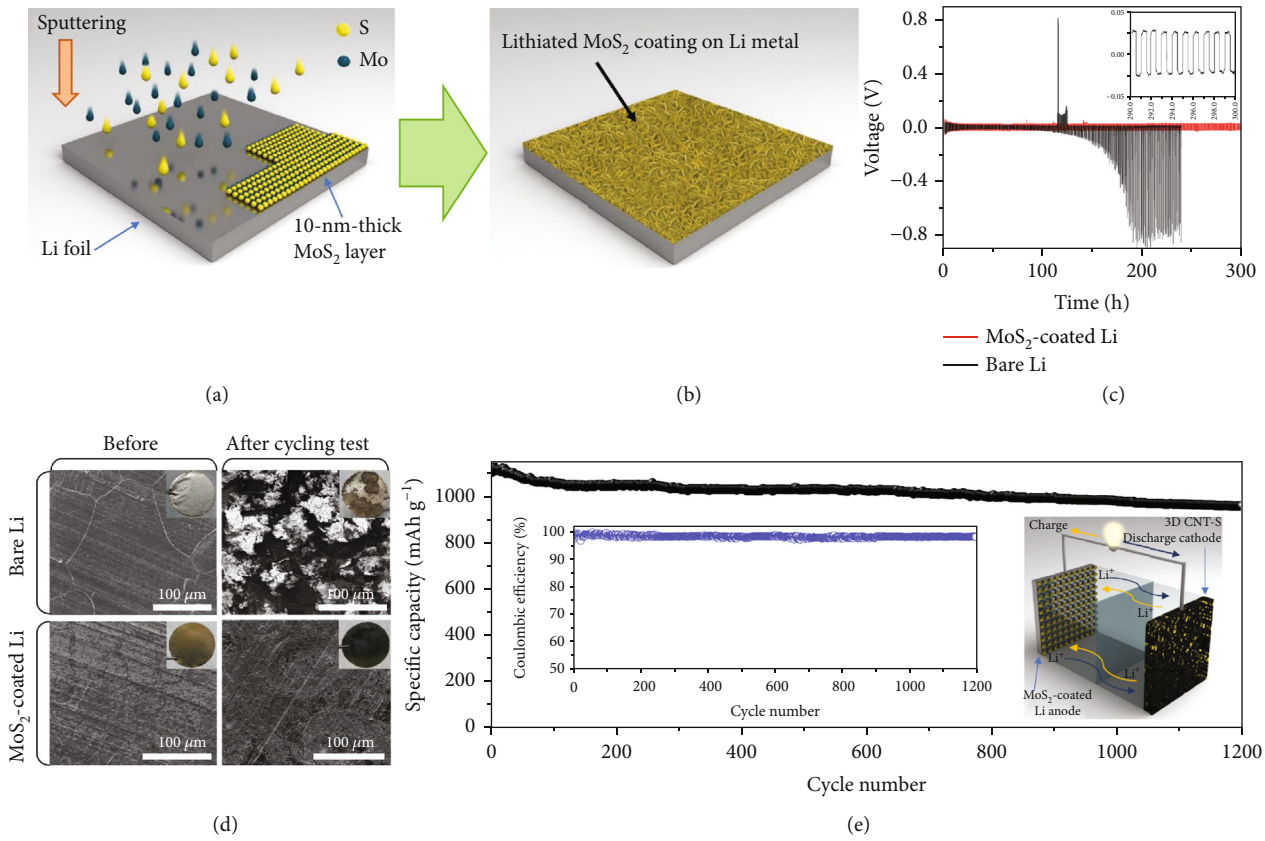


FIGURE 10: (a) The sputtering and (b) subsequent lithiation of MoS_2 for the modification of the Li anode. (c) Voltage-time profiles of symmetric cells using bare Li and MoS_2-modified Li as anodes tested under 10.0 mA cm^{-2}. Inset is the magnified voltage-time profile for the MoS_2-modified Li anode. (d) The SEM and photo (inset) images of bare Li and MoS_2-modified Li during cycling at 10.0 mA cm^{-2}. (e) The stability of the Li-S cell composed of the MoS_2-modified Li anode and CNT-S cathode cycling over 1200 times at 0.5 C. Insets are the Coulombic efficiency (left) and schematic kinetics of the Li-S battery. (a–e) Reproduced with permission from Nature [82].

conversion) and Li^+ migration (suppressing Li dendrites) than 2H. However, the adsorption capability of molybdenum dichalcogenides is moderate compared to that of molybdenum oxides. Moreover, the synthesis of 1T phase molybdenum dichalcogenides usually requires complex procedures involving ion intercalation, heteroatom doping, and utilization of explosive reagents.

4. Molybdenum Nitrides

Transition metal nitrides are widely adopted as a catalyst for sensing and electroanalysis applications for their superior reactivity and chemical robustness [33, 88–90]. In contrast to their counterparts of oxides (1×10^{-3} S m^{-1}) and sulfides ($9.7 \times 10^{-2} - 10^3$ S m^{-1}) [49, 91], molybdenum nitrides possess improved electronic conductivity. Utilizing silica as the template (Figures 12(a) and 12(b)), Jiang et al. prepared highly conductive mesoporous Mo_2N (1×10^5 S m^{-1}, 121 m^2 g^{-1}) with an average pore size of 8.6 nm [92]. When mesoporous Mo_2N were immersed into Li_2S_6 solution, the yellow color disappeared, suggesting its strong adsorption. Benefiting from these merits, the mesoporous Mo_2N/S cathode showed high capacity retention of 92.0% (corresponding to 914 mAh g^{-1}) after charged/discharged at 0.5 C for 100 cycles, better than that based on nonporous Mo_2N. Similarly, Wang et al. synthesized the MoN@N-doped carbon (MoN-NC) porous octahedron using MOF ($[Cu_2(BTC)_{4/3}(H_2O)_2]_6[H_3PMo_{12}O_{40}]$; BTC (benzene-1,3,5-tricarboxylate)) as precursors followed by thermal annealing, etching, and nitridation at elevated temperature (Figure 12(c)) [93]. The CV results tested in a symmetric cell using the Li_2S_6-containing electrolyte indicated MoN-NC promoted the chemisorption and conversion of LiPSs. The MoN-NC/S cathode with 77.0 wt% sulfur loading had 88.0% capacity retention at 0.5 C with 934 mAh g^{-1} left after 100 cycles, superior to MoN/S (71.0%) and NC/S (49.0%).

The design of heterostructures is another viable way to enhance the performance of molybdenum nitrides. Ye et al. prepared the 2D MoN-VN nanosheets (~7.1 nm thick) with a lateral size of a few microns via a salt template method and employed them as the sulfur host to regulate LiPSs (Figures 12(d)–12(g)) [94]. The introduction of V atoms can tailor the electronic states of Mo sites on the MoN surface and enabled higher adsorption ability for V-MoN than MoN. The MoN-VN/S cathode demonstrated capacity retention of 72.0% with 555 mAh g^{-1} left after cycling at 1 C for 500 times.

Yang et al. developed an in situ topotactical nitridation strategy to prepare MoO_2-Mo_2N nanobelts that were incorporated as interlayer materials between the cathode and the separator in Li-S batteries (Figure 13) [95]. DFT calculation

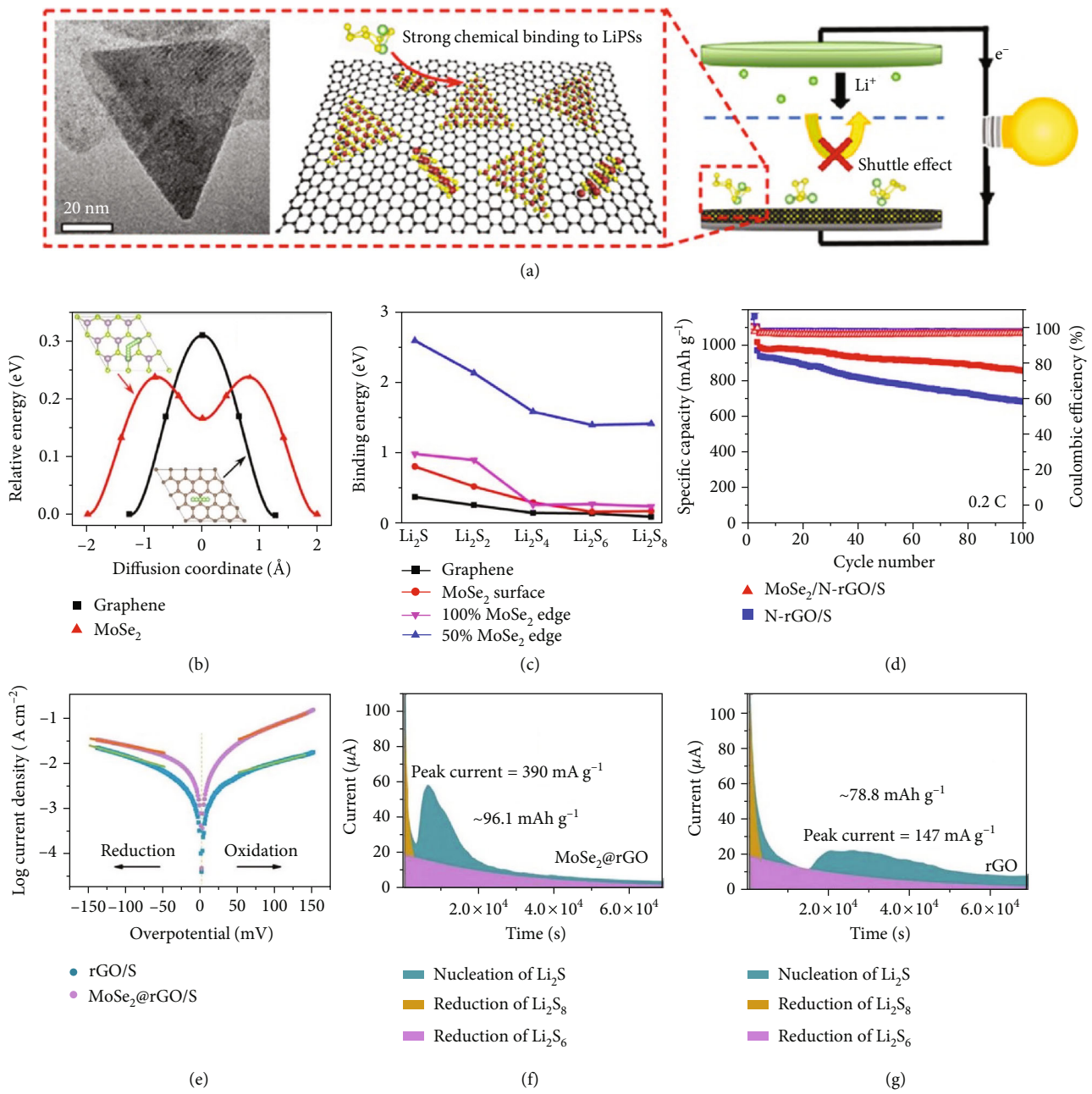


FIGURE 11: (a) Schematic of the $MoSe_2$ on nitrogen-doped reduced GO ($MoSe_2$/N-rGO) and its strong chemical binding to LiPSs. (b) Energy profile of Li atom diffusion on graphene and $MoSe_2$ surfaces. (c) Binding energy of Li_2S_n on the graphene surface, $MoSe_2$ surface, 100% $MoSe_2$ edge, and 50% $MoSe_2$ edge. (d) Cycling stability of $MoSe_2$/N-rGO/S and N-rGO/S. (a–d) Reproduced with permission from the American Chemical Society [83]. (e) The Tafel plots of the $MoSe_2$@rGO/S and rGO/S cathodes. The discharge behavior of Li_2S_8 on (f) $MoSe_2$@rGO and (g) rGO at 2.05 V. (e–g) Reproduced with permission from Wiley-VCH [84].

disclosed that the binding strength of MoO_2 surfaces to Li_2S_4 is higher than that of Mo_2N. The potentiostatic discharge tests of Li-Li_2S_8 batteries based on MoO_2-Mo_2N at 2.08 V exhibited a capacity of ~202 mAh g^{-1} for Li_2S precipitation, better than that based on MoO_2 (~103 mAh g^{-1}) and Mo_2N (~118 mAh g^{-1}), confirming the accelerated conversion of LiPSs. Such heterostructures retained 73.6% (823 mAh g^{-1}) after 300 cycles at 0.5 C. In another work, Li et al. proposed heterostructural MoO_2-Mo_3N_2 holey nanobelts which exhibited improved electrochemical kinetics compared with their single-component counterparts (MoO_2 or Mo_3N_2) [96]. This noncarbon heterojunction substrate enabled a high loading level of 75.0 wt% sulfur. The initial capacity of MoO_2-Mo_3N_2/S with 75.0 wt% of sulfur loading retained 762 mAh g^{-1} (corresponding to 76.0% of initial capacity) after cycling at 0.5 C for 1000 times. Alternatively, Chen et al. coated molybdenum nitride nanosheets, which were obtained through a salt template method, on the Celgard separator

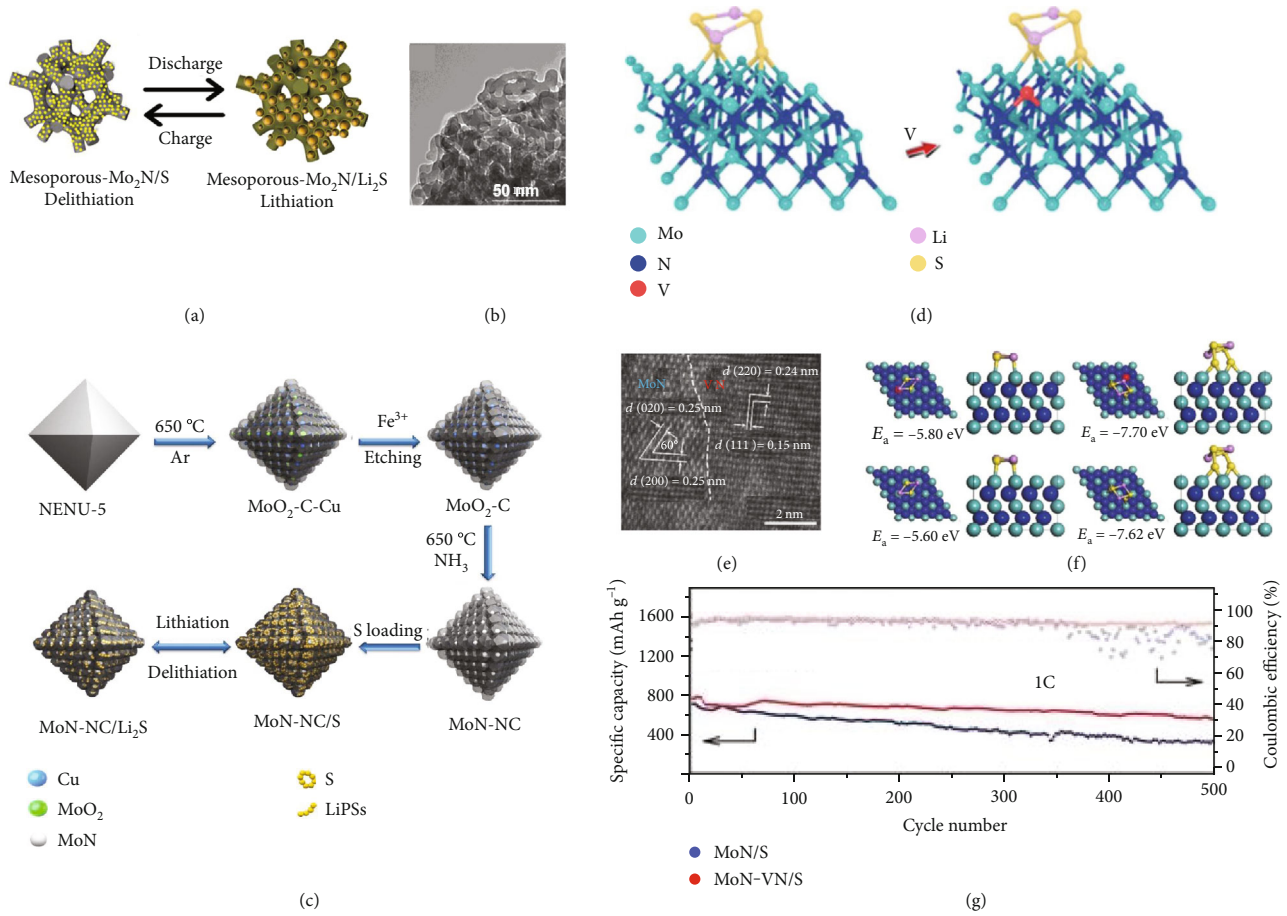


FIGURE 12: (a) The charge/discharge process of the mesoporous Mo_2N/S cathode. (b) TEM image of mesoporous Mo_2N. (a, b) Reproduced with permission from Elsevier [92]. (c) Synthesis of MoN-NC. Reproduced with permission from the Royal Society of Chemistry [93]. (d) The model of the 2D MoN-VN heterostructure. (e) The scanning transmission electron microscopy (STEM) image of the MoN-VN. (f) Optimized configurations and binding energies of V-MoN-Li_2S_2, V-MoN-Li_2S_4, MoN-Li_2S_2, and MoN-Li_2S_4, respectively. (g) Cycling performances and CE of MoN/S and MoN-VN/S cathodes. (d–g) Reproduced with permission from Wiley-VCH [94].

(denoted as MoN_x/Celgard), and the as-assembled Li-S batteries delivered a capacity of 566 mAh g^{-1} after 500 cycles at 0.5 C, corresponding to 68.1% retention [97].

Very recently, the Mo_2N@CNF matrix was prepared by thermally annealing the hybrid film of CNF and $(NH_4)_6Mo_7O_{24}$•$4H_2O$ at 800°C and then used as a scaffold for homogenous Li plating (Figure 14(a)) [98]. The XPS spectrum of Mo 3d in lithiated Mo_2N@CNF after etched by Ar plasma unveiled that Mo_2N reacted with Li generating Mo metal and Li_3N via $3Li + Mo_2N \rightarrow 2Mo + Li_3N$ (Figure 14(b)). In addition to the matchable lattice between Li and Mo, a theoretical calculation based on crystal orbital Hamilton population (COHP) indicated that Li tends to bond with Mo rather than Li due to the higher strength (Figure 14(c)), resulting in the uniform nucleation and subsequent deposition of Li. The incorporation of Mo_2N@CNF enabled the symmetric cell outstanding cycling stability at 6 mA cm^{-2} for 1500 h (Figure 14(d)).

Molybdenum nitrides have excellent electrical conductivity, high catalytic properties, and robust structure, which are beneficial for accelerating the conversion of LiPSs and alleviating electrode fragmentation caused by the volume expansion of the sulfur cathodes. Furthermore, their unique lithophilicity can guide the homogeneous electrodeposition of Li metal, thereby alleviating the dendritic growth. However, similar to molybdenum oxides, molybdenum nitrides generally have low specific surface areas and lack a facile synthetic strategy [33].

5. Molybdenum Carbides

Owing to its high catalytic activity, low cost, and good conductivity, molybdenum carbide has been widely studied during the past decades for catalysis [33, 121]. Chen et al. synthesized porous Mo_2C-C with a surface area of 196 m^2 g^{-1} through pyrolyzing Mo-based MOF at 800°C followed by $FeCl_3$ etching (Figure 15(a)) [109]. The hybrid showed effective adsorption to LiPSs while the ultrafine β-Mo_2C nanocrystals encapsulated in carbon accelerated the redox kinetics toward LiPS conversion. As a result, the Mo_2C-C NO/S cathode containing ~1.1 mg cm^{-2} sulfur delivered a capacity of 762 mAh g^{-1} (72.5% of the initial value) after the cycling test at 1 C for 600 times. Razaq et al. anchored Mo_2C nanoparticles on carbon nanotubes (CNT/Mo_2C) by

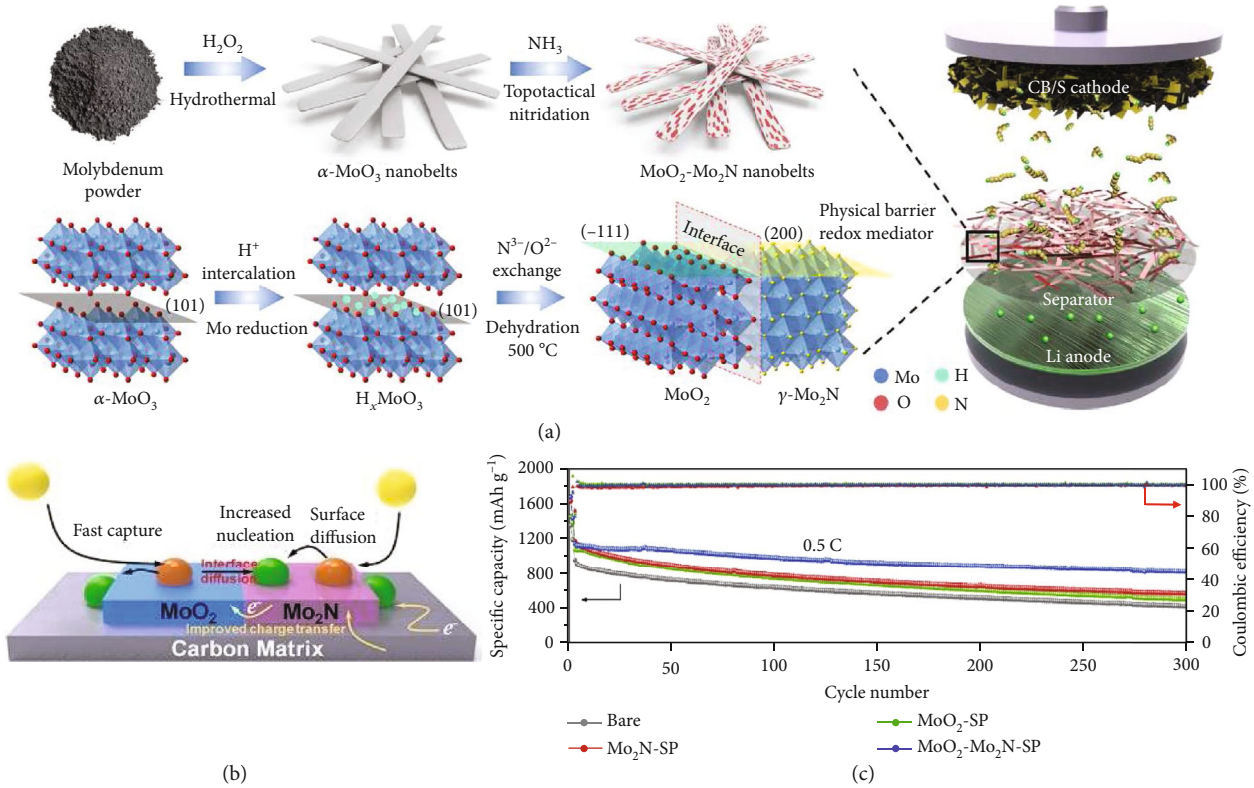


FIGURE 13: (a) Schematic illustration of the synthesis of the MoO_2-Mo_2N heterostructure. (b) The conversion of LiPSs and the nucleation of Li_2S on the MoO_2-Mo_2N surface. (c) Cycling performance of the cells based on different separators. (a–c) Reproduced with permission from Elsevier [95].

annealing the mixture of CNTs and ammonium molybdate at 800°C (Figures 15(b) and 15(c)) [120]. The strong binding between Mo_2C and CNTs ensured a highly conductive pathway for efficient electron transfer, and the porous assembly guaranteed rapid electrolyte infiltration, while the combination (CNT/Mo_2C) prompted redox reactions of LiPSs. At 2 C, CNT/Mo_2C/S exhibited 417 mAh g^{-1} (corresponding to capacity retention of 52.0%) after cycling 900 times. Similarly, Shang et al. achieved a device capacity of 1086 mAh g^{-1} at 0.2 C by decorating Mo_2C nanoparticles on N-doped carbon nanofibers (Mo_2C-NCNF) as the sulfur host for Li-S batteries [107]. Li et al. embedded necklace-like MoC in N-doped carbon nanofibers (MoC@N-CNF) using bacterial cellulose as a carbon source. The as-fabricated MoC@N-CNF/S cathode containing 10.0 mg cm^{-2} sulfur provided a capacity of 911 mAh g^{-1} at 1 C retaining 70.6% after 350 cycles.

Apart from the application as the cathode host in suppressing the shuttle effect, the lithiophilic Mo_2C also has the ability to facilitate the uniform Li deposition on anodes. In a recent work, an interlayer between the separator and the anode was prepared by uniformly anchoring Mo_2C quantum dots (MQDs) on N-doped graphene (MQD@NG) under the assistance of poly(oxypropylene) diamines (D_{400}) (Figure 16(a)) [113]. The experimental results demonstrated that the presence of the MQD@NG interlayer effectively suppressed the Li dendrites. In contrast to the PP separator, the lithiophilic MQD@NG-modified PP separator possessing fast ion diffusion pathways promoted uniform Li^+ flow to the surface of Li metal anodes, leading to homogeneous dendrite-free Li deposition. As a result, the Li|Li symmetric cell with the MQD@NG/PP separator showed stable voltage-time profiles with small hysteresis over 800 h at 5 mA cm^{-2} and 1 mAh cm^{-2}, better than that composed of the bare PP separator (130 h) and G/PP (~200 h).

Molybdenum carbides have similar properties to molybdenum nitrides with excellent metallic conductivity, high catalytic activity for LiPS conversion, good affinity to Li for uniform plating, yet generally low specific surface areas [33]. In addition, The preparation of molybdenum carbides typically involves high-temperature calcination under a reductive or inert atmosphere, making the process costly and complicated.

6. Molybdenum Phosphides

Transition metal phosphides (TMPs) are a kind of widely utilized active materials in catalysis and energy storage for their high conductivity and stability [122, 123]. Particularly, molybdenum phosphide is a well-known catalyst for the hydrodesulfurization process in the petroleum industry because of its chemical interaction with sulfur species [124, 125]. Inspirited by this principle, Yang et al. synthesized the MoP-CNT hybrid by hydrolysis of $(NH_4)_6Mo_7O_{24}$ to MoO_x followed by phosphorization in PH_3 and verified the electrocatalytic properties of MoP nanoparticles (Figures 17(a)–17(c)) [126]. The MoP-CNT/S cathode containing 10.0 wt%

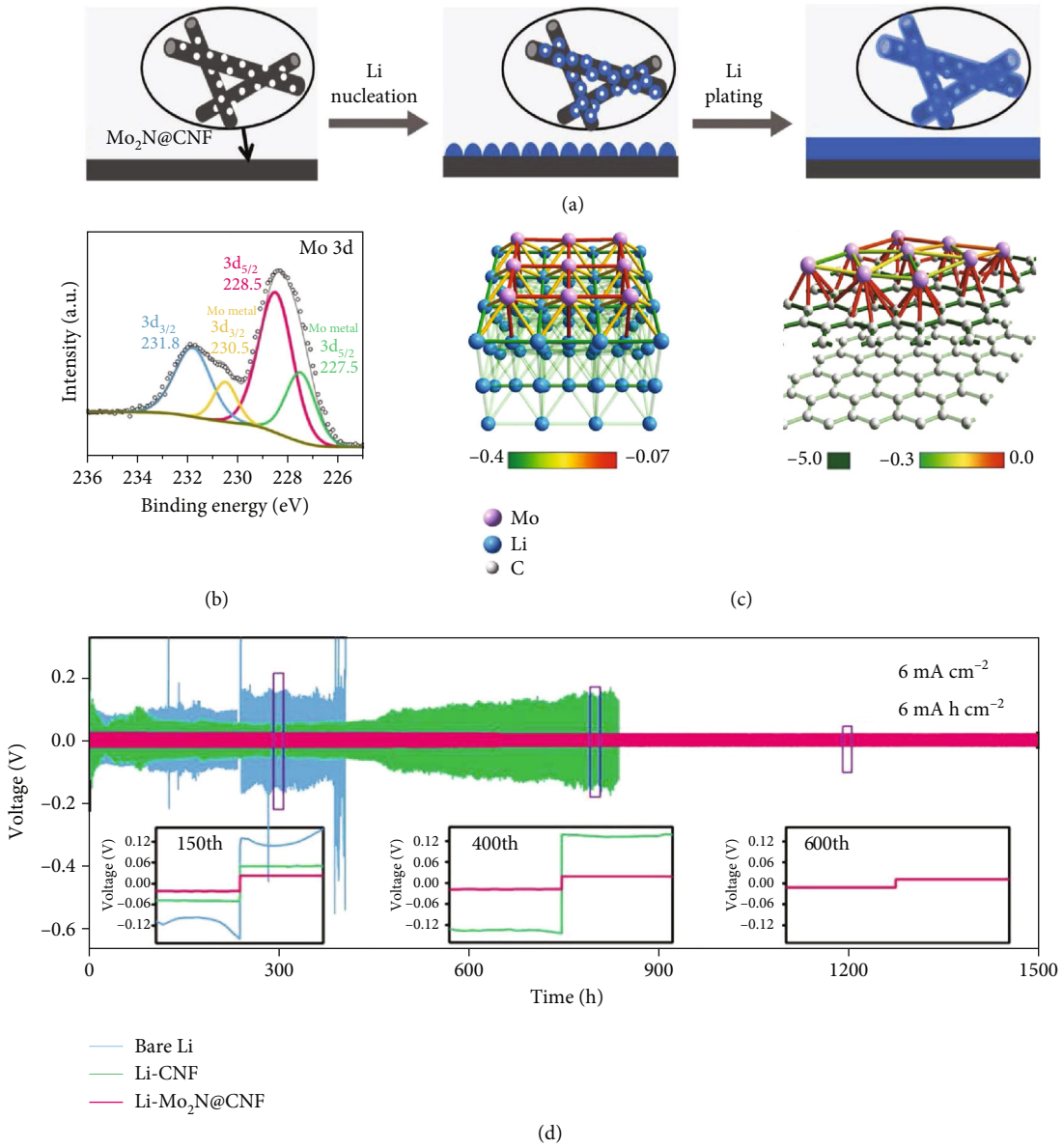


Figure 14: (a) The nucleation and subsequent plating process on Mo_2N@CNF. (b) XPS spectrum of Mo 3d in lithiated Mo_2N@CNF after bombarded by Ar plasma for 5 min. (c) Theoretical calculation of the interatomic interaction between Mo-Li (left) and C-Li (right) by using the crystal orbital Hamilton population (COHP). (d) Cycling tests of the symmetric cells composed of bare Li, Li-CNF, and Li-Mo_2N@CNF anodes at 6 mA cm^{-2}. (a–c) Reproduced with permission from Wiley-VCH [98].

of MoP-CNT showed a capacity of ~830 mAh g^{-1} without any obvious decay over 50 cycles at 0.8 mA cm^{-2}.

Phase engineering and heteroatom doping are considered two effective strategies to adjust the properties of the catalyst [128, 129]. Following this idea, Ma et al. transformed MoP to Mo_4P_3 via Ru doping (Ru-Mo_4P_3) and demonstrated that Ru-Mo_4P_3 can effectively facilitate the electrocatalytic conversion of LiPSs (Figures 17(c)–17(f)) [127]. The separation between the cathodic and anodic peaks was ~0.18 V for the devices composed of HCS-Ru-Mo_4P_3, suggesting an accelerated LiPS conversion. The enhanced catalytic activity was attributed to two aspects: (i) compared to MoP, the Mo/P ratio in Mo_4P_3 became higher, exposing more Mo sites, and (ii) the Ru doping optimized the adsorption/desorption of reaction intermediates on Mo sites [130–132]. The HCS-Ru-Mo_4P_3/S cathode delivered 1178 mAh g^{-1} and 660 mAh g^{-1} at 0.5 C and 4 C in the Li-S battery, respectively.

By drop casting molybdenum diphosphide (MoP_2) nanoparticles on superaligned CNT films that were cross-stacked together, Luo et al. designed a multifunctional interlayer on the Celgard 2400 separator (Figure 18) [116]. According to X-ray photoelectron spectroscopy (XPS) characterization, when the battery was discharged to 2.08 V, Mo^{4+} in the Mo 3d spectrum was detected, suggesting that the oxidation of Li_2S_4 to thiosulfate may be accomplished by Mo^{6+}. Li_2S_4 and Li_2S_2 Raman peaks were only observed on the side of

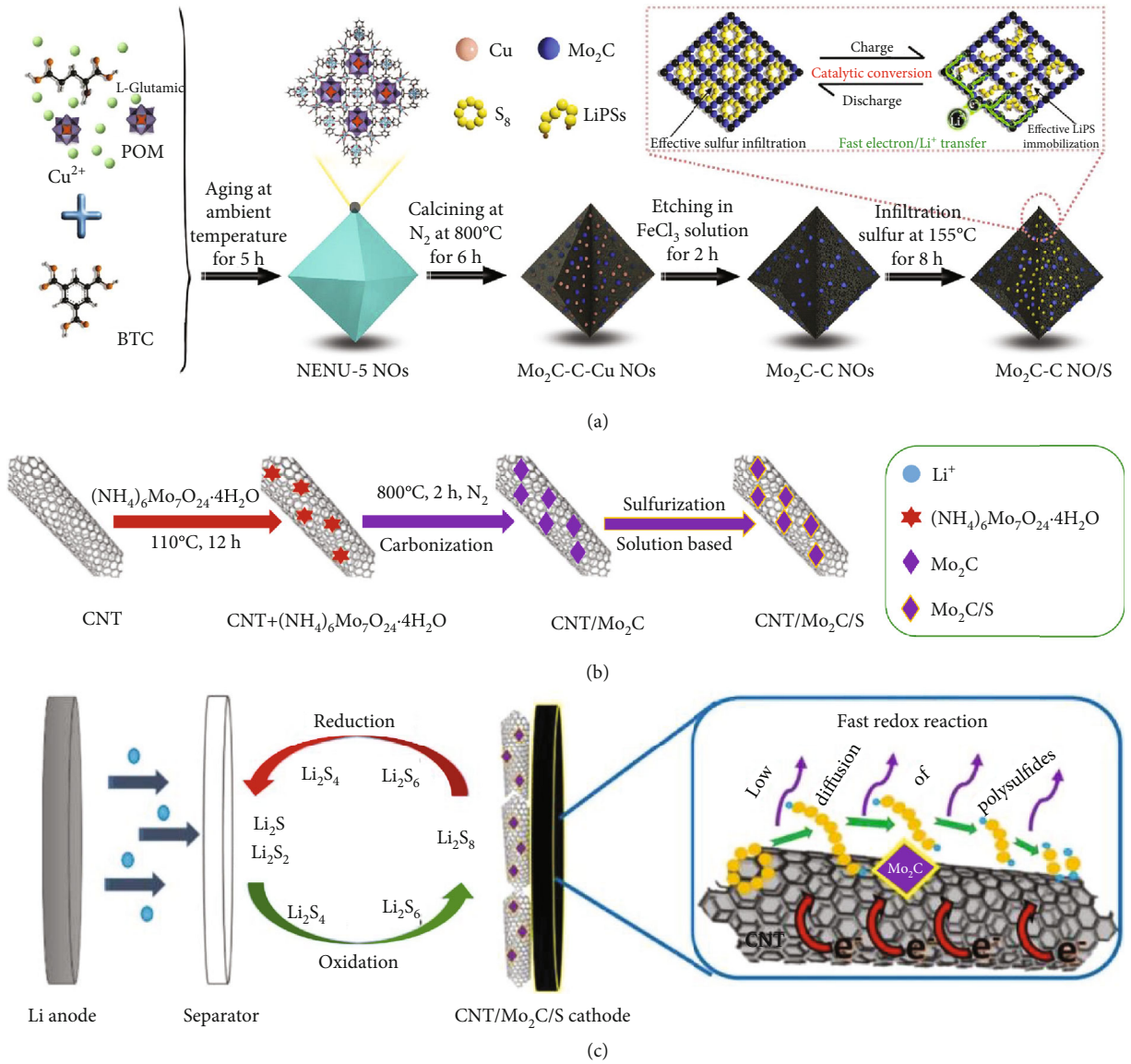


Figure 15: (a) The preparation of the MoC_2-C NO/S cathode. Reproduced with permission from Elsevier [109]. (b) Schematic illustration of the synthesis of CNT/Mo_2C and CNT/Mo_2C/S. (c) Fast conversions of LiPSs on CNT/Mo_2C via adsorption and subsequent redox reaction. (b, c) Reproduced with permission from IOP Publishing [120].

the CNT/MoP_2 interlayer facing to the cathode, indicating that LiPSs were effectively blocked because of the physical hindrance of CNT films and the catalytic contribution of Mo sites. This was further confirmed by DFT calculations, which showed that high-order LiPSs (Li_2S_4 and Li_2S_8) had much larger binding energy to Mo sites in comparison with P sites. The CNT/MoP_2 modification enabled the as-fabricated Li-S battery 1223 mAh g^{-1} discharging capacity at 0.2 C with retention of 74.0% after 100 cycles.

Molybdenum phosphides comparably exhibit superior catalytic performance for the catalytic conversion of LiPSs even under lean electrolyte conditions, which is beneficial to increase the energy density of Li-S batteries. The Mo centers are believed to be the active sites for the adsorption and electrocatalytic conversion of LiPSs. Although molybdenum phosphides can be synthesized under a relatively mild condition, compared with molybdenum carbides and molybdenum nitrides, using $NH_4H_2PO_4$ and NaH_2PO_2 as the P sources, toxic gas (e.g., PH_3) is generated during phosphorization and phosphates are inclined to be oxidized in air.

7. Molybdenum Metal

Very recently, Li et al. prepared a Mo/CNT thin film by a magnetron sputtering technique and used it as an interlayer in Li-S batteries (Figure 19) [118]. It was claimed that the sulfur-passivated Mo nanoclusters (~0.05 mg cm^{-2}) in Mo/CNTs acted as capturing sites and catalytic centers for the chemical immobilization and conversion of LiPSs, while the compact CNT film functioned as a physical blocker for

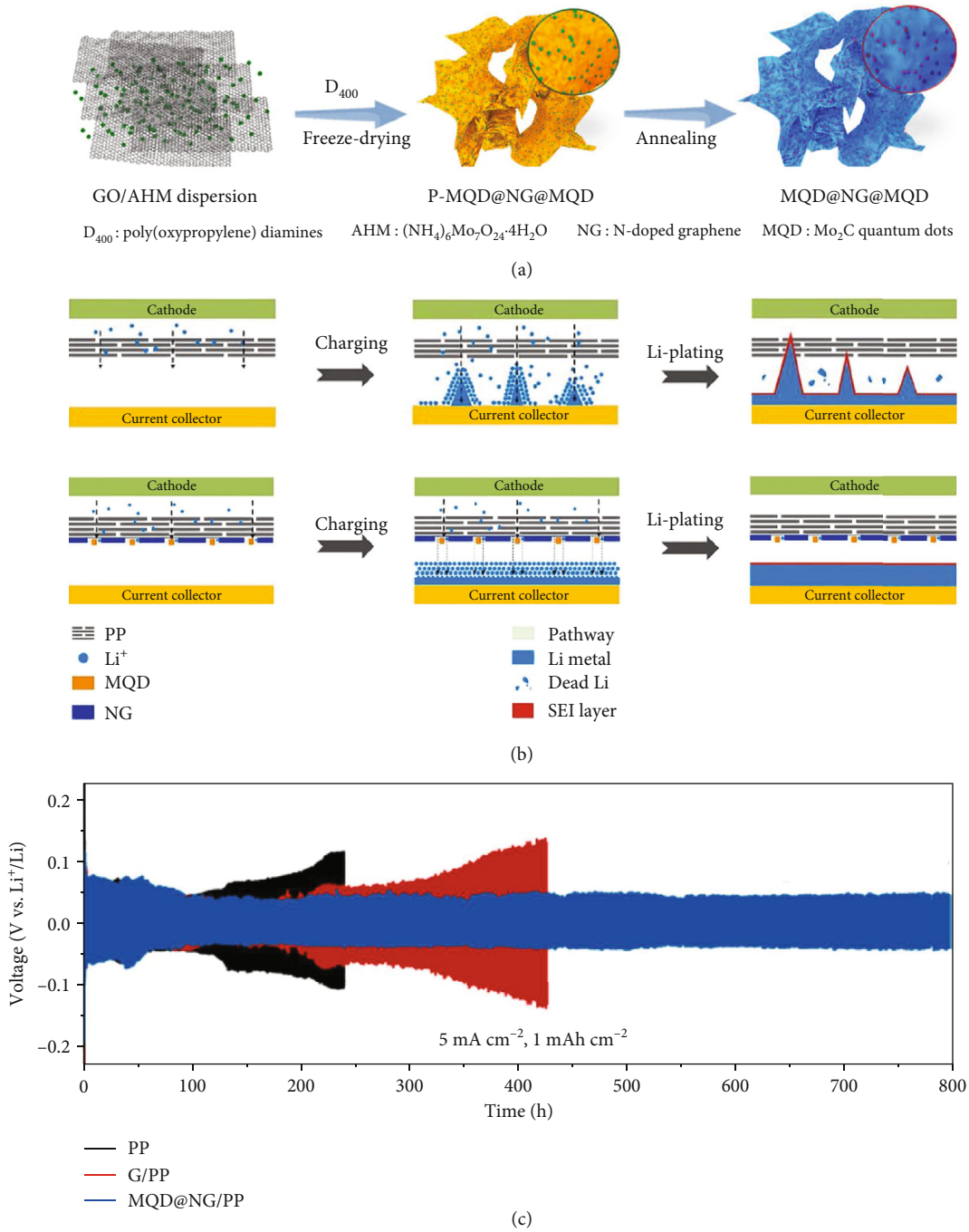


Figure 16: (a) The loading of Mo_2C quantum dots (MQDs) on N-doped graphene (NG) under the assistance of poly(oxypropylene) diamines (D_{400}). (b) Li plating process in Li-S batteries, respectively, using PP and MOD@NG/PP separators. (c) Voltage-time profiles of symmetric cells, respectively, using PP, G/PP, and MOD@NG/PP separators at 5 mA cm^{-2} (1 mAh cm^{-2}). Reproduced with permission from Elsevier [113].

inhibiting the LiPS shuttle. As a result, the battery self-discharge was effectively suppressed and 722 mAh g^{-1} was achieved at 1 C with 65.0% retained after 500 cycles.

To date, there are only a few works reporting the direct utilization of Mo metal in Li-S batteries. According to these works of literature, the adsorption and catalytic properties of Mo metal are attributed to the formation of Mo-S bonds, yet further pieces of evidence are required. In addition, the binding energy theoretically follows the sequence of Mo-Mo>Mo-Li>Li-Li [98]. Therefore, the uniform loading of Mo nanoparticles on a high specific surface substrate may have the potential for the protection of Li metal anodes.

8. Conclusions and Prospects

We have comprehensively summarized the recent progress on Mo-based materials for Li-S batteries. Comparably, molybdenum oxides show strong adsorption capability

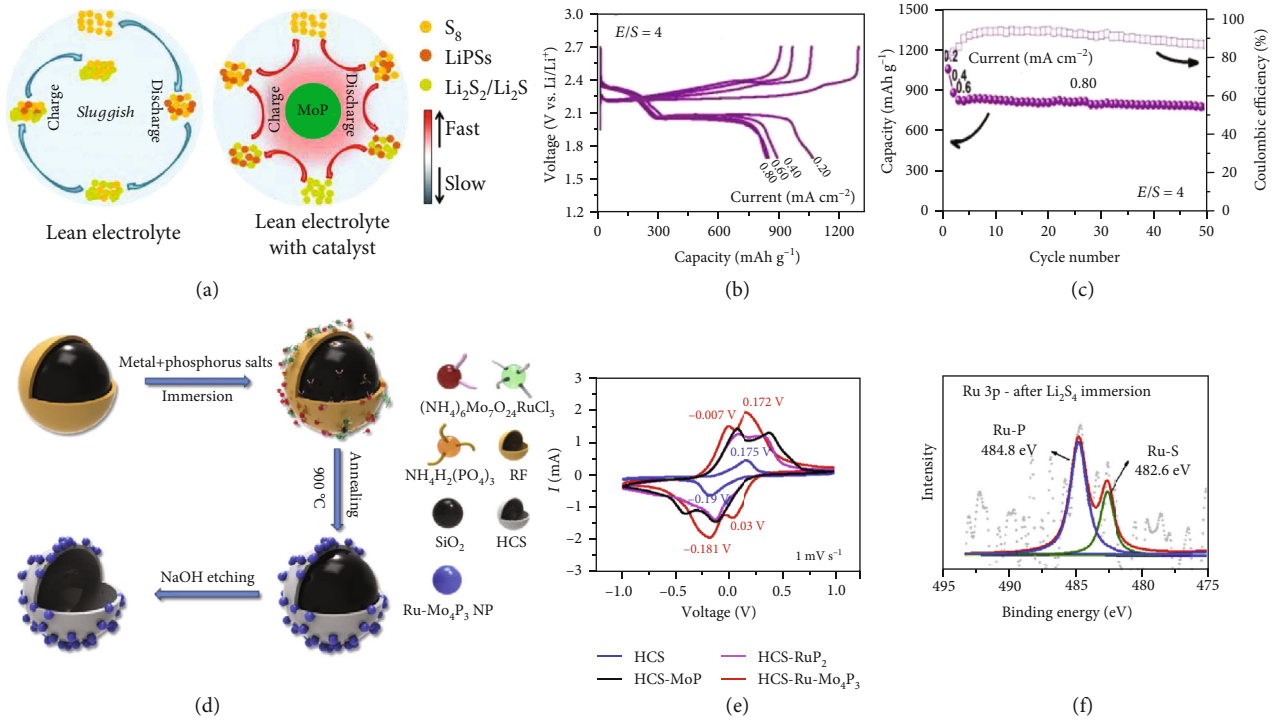
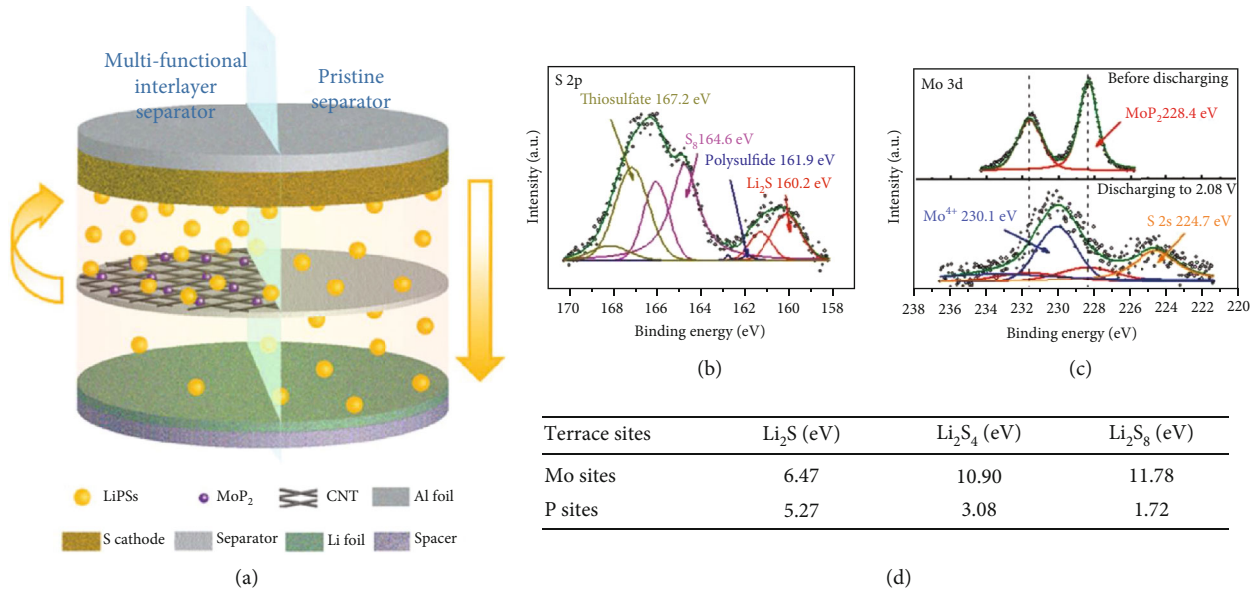


FIGURE 17: (a) Schematic illustrations of possible reaction pathways for sulfur cathodes with and without the MoP catalyst under lean electrolyte condition. (b) Representative charge/discharge curves at various rates and (c) stability test of the MoP-CNT/S electrode under the $E/S = 4$ condition. (a–c) Reproduced with permission from Wiley-VCH [126]. (d) The preparation of HCS-Ru-Mo_4P_3 NPs. (e) CV profiles of the asymmetric cells based on HCS, HCS-MoP, HCS-RuP_2, and HCS-Ru-Mo_4P_3 hosts with 0.1 M Li_2S_8 in the catholyte. (f) The XPS spectra of Ru 3p in HCS-Ru-Mo_4P_3 after Li_2S_4 immersion. (d–f) Reproduced with permission from Elsevier [127].



Terrace sites	Li_2S (eV)	Li_2S_4 (eV)	Li_2S_8 (eV)
Mo sites	6.47	10.90	11.78
P sites	5.27	3.08	1.72

(d)

FIGURE 18: (a) Li-S cells with (left) and without (right) the modification of MoP_2/CNT on commercial separators. XPS spectra of (b) S 2p and (c) Mo 3d in CNT/MoP_2 before and after cycling. (d) The calculated binding energies between MoP_2 and different LiPSs. (a–d) Reproduced with permission from Wiley-VCH [116].

toward LiPSs due to their polar Mo-O bond. However, the reaction kinetics of absorbed LiPSs are lowered by their poor intrinsic conductivity. Comparably, molybdenum dichalcogenides have improved conductivity, moderate binding energy, and catalytic performance with active centers mainly concentrating at the edge and defect sites. Molybdenum nitrides, carbides, and phosphides possess high electronic conductivity, excellent catalytic properties, and chemical

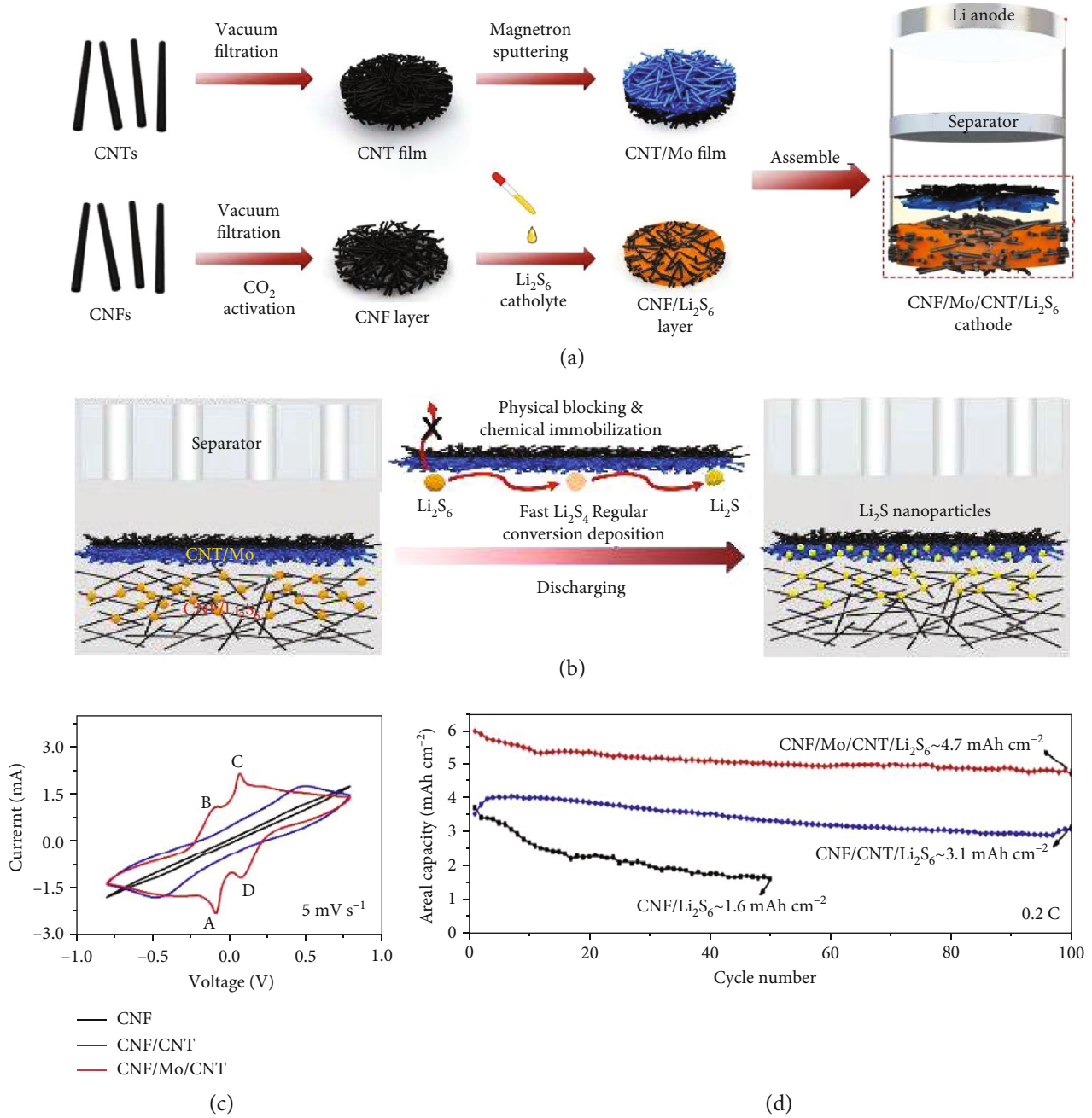


Figure 19: (a) The assembly of the Li-S battery based on the CNF/Mo/CNT/Li_2S_6 cathode. (b) The electrochemical behavior of the CNF/Mo/CNT/Li_2S_6 cathode with the Li_2S_6 catholyte. (c) CV curves of the symmetric cells employing CNF/Mo/CNT, CNF/CNT, and CNF electrodes at 5 mV s^{-1}. (d) Cycling performances of Li-S batteries based on CNF/Mo/CNT/Li_2S_6, CNF/CNT/Li_2S_6, and CNF/Li_2S_6 electrodes under a high sulfur mass loading (7.6 mg cm^{-2}). (a–d) Reproduced with permission from the American Chemical Society [118].

durability in the organic electrolyte (without reacting with Li), which are promising materials for capturing LiPSs and catalyzing their redox reaction. Moreover, these materials as a scaffold facilitate the uniform deposition of insoluble Li_2S, thus alleviating the shuttle effect. Furthermore, the unique lithophilicity of molybdenum nitrides and carbides facilitates the uniform electroplating of Li metal, thereby alleviating the dendritic growth of Li metal anodes. Although their catalytic performance can be further enhanced by reducing particle sizes so as to expose more electrochemical active surfaces, complicated procedures and harmful gases (e.g., NH_3 and PH_3) are inevitably involved. Mo metal shows the highest electronic conductivity and moderate catalytic activity (probably due to the formation of Mo-S bonds) toward the conversion of LiPSs. However, Mo metal can be oxidized by O_2 in air and react with sulfur species during the charge/discharge process, forming MoO_x and Mo-S bonds on its surface, thereby hindering the electron transport during the reaction [39].

Table 1: The applications of Mo-based materials in Li-S batteries.

Classification		Material	Preparation method (design strategies)	Structure characteristics	Sulfur content (wt%), areal sulfur loading (mg cm^{-2}), areal loading on the separator (mg cm^{-2})	Electrolyte dosage (μL mg^{-1})	Retained capacity (mAh g^{-1}), capacity retention (%), cycle number, and rate (C)	Voltage range (V)	Reference
Molybdenum oxides	Cathode	MoO_3/CNT/S	Alternative filtration (hybridizing with carbonaceous materials)	Double-layer membrane	28.8 wt%, 1.0 mg cm^{-2}, N/A	N/A	666 mAh g^{-1}, 62.0%, 350, 0.5 C	1.8–2.8 V	[52]
		MoO_{3-x}/S	Hydrothermal reaction and annealing (introducing oxygen defects)	Nanobelt	47.0 wt%, 1.0 mg cm^{-2}, N/A	N/A	480 mAh g^{-1}, 62.0%, 600, 1 C	1.7–2.6 V	[47]
		$Sn_{0.063}MoO_3$/S	Solvothermal reaction (intercalating heteroatoms)	Nanoribbon	67.4 wt%, ~1.3 mg cm^{-2}, N/A	N/A	721 mAh g^{-1}, 80.0%, 500, 1 C	1.8–2.8 V	[48]
		MoO_3-CP/S	Hydrothermal reaction (hybridizing with carbonaceous materials)	Nanoflake	N/A, 3.0 mg cm^{-2}, N/A	N/A	976 mAh g^{-1}, 99.5%, 1000, 1 C	1.7–2.8 V	[99]
		MoO_2/C-NC/S	Calcination and etching (constructing nanostructure by MOF template)	Porous framework	76.3 wt%, 1.1 mg cm^{-2}, N/A	N/A	400 mAh g^{-1}, 52.7%, 1000, 2 C	1.7–2.8 V	[60]
		MoO_2/G/S	Hydrothermal reaction and annealing (constructing nanostructure)	Hollow sphere	79.0 wt%, N/A, N/A	N/A	905 mAh g^{-1}, 80.5%, 100, 0.2 C	1.7–2.8 V	[59]
		MoO_2/S	Calcination and etching (constructing nanostructure by silicon template)	Mesoporous framework	38.0 wt%, 1.0 mg cm^{-2}, N/A	N/A	570 mAh g^{-1}, 51.8%, 250, 0.1 C	1.7–2.8 V	[100]
	Separator	MoO_3@CNT	Hydrothermal reaction and filtration (hybridizing with carbonaceous materials)	Scaffold-like network	N/A, 0.6 mg cm^{-2}, ~0.6 mg cm^{-2}	N/A	755 mAh g^{-1}, 53.0%, 200, 0.3 C	1.5–3.5 V	[54]
		MoO_3 separator	Hydrothermal reaction and slurry coating (constructing nanostructure)	Porous nanobelt layer	N/A, 1.0 mg cm^{-2}, ~0.5 mg cm^{-2}	N/A	684 mAh g^{-1}, 49.0%, 200, 0.5 C	1.6–2.8 V	[53]
		MoO_2-CNF	Electrospinning and calcination (hybridizing with carbonaceous materials)	Mesoporous nanofiber membrane	70.0 wt%, 2.5 mg cm^{-2}, N/A	38 μL mg^{-1}	1006 mAh g^{-1}, 73.6%, 150, 0.1 C	1.7–2.8 V	[63]
		MoO_3/CNF	Electrospinning and calcination (hybridizing with carbonaceous materials)	Mesoporous nanofiber membrane	N/A, N/A, N/A	N/A	776 mAh g^{-1}, 55.0%, 500, 0.5 C	1.7–2.7 V	[55]

Table 1: Continued.

Classification		Material	Preparation method (design strategies)	Structure characteristics	Sulfur content (wt%), areal sulfur loading ($mg\,cm^{-2}$), areal loading on the separator ($mg\,cm^{-2}$)	Electrolyte dosage ($\mu L\,mg^{-1}$)	Retained capacity ($mAh\,g^{-1}$), capacity retention (%), cycle number, and rate (C)	Voltage range (V)	Reference
Molybdenum sulfide	Cathode	MoS_{2-x}/rGO/S	Filtration and calcination (introducing sulfur defects)	Nanoflake	75.0 wt%, 0.9 $mg\,cm^{-2}$, N/A	55 $\mu L\,mg^{-1}$	820 $mAh\,g^{-1}$, 70.6%, 150, 0.5 C	1.8–2.6 V	[71]
		P-$Mo_{0.9}Co_{0.1}S_2$/S	Hydrothermal reaction (introducing heteroatoms)	Core-shell nanotube	N/A, 2.0 $mg\,cm^{-2}$, N/A	N/A	1187 $mAh\,g^{-1}$, 89.0%, 150, 0.5 C	1.7–2.6 V	[72]
		GA-DR-MoS_2/S	Hydrothermal reaction and freeze-drying (constructing nanostructure by ice template)	Porous 3D aerogel	70.0 wt%, N/A, N/A	N/A	821 $mAh\,g^{-1}$, 57.8%, 500, 0.2 C	1.7–2.8 V	[78]
		rGO-MoS_2 QD/S	Hydrothermal reaction (constructing nanostructure)	Quantum dot	50.0 wt%, ~1.4 $mg\,cm^{-2}$, N/A	15 $\mu L\,mg^{-1}$	503 $mAh\,g^{-1}$, 99.3%, 300, 2 C	1.8–2.8 V	[101]
		MoS_2/S	Intercalation exfoliation and electrostatic assembly (constructing nanostructure)	Hollow sphere	65.0 wt%, 1.5 $mg\,cm^{-2}$, N/A	N/A	585 $mAh\,g^{-1}$, 44.9%, 1000, 1 C	1.8–2.6 V	[102]
		MoS_2/CNT/S	Drop casting (hybridizing with carbonaceous materials)	Cross-stacked membrane	N/A, 2.6 $mg\,cm^{-2}$, N/A	N/A	855 $mAh\,g^{-1}$, 58.0%, 50, 0.2 C	1.5–2.8 V	[103]
		MoS_2/g-C_3N_4/S	Recrystallization and calcination (hybridizing with polar materials)	Nanosheet	59.0 wt%, 1.5 $mg\,cm^{-2}$, N/A	18 $\mu L\,mg^{-1}$	569 $mAh\,g^{-1}$, 73.2%, 400, 1 C	1.8–2.8 V	[104]
		Edg-MoS_2/C HMs	Hydrothermal reaction and calcination (constructing nanostructure)	Hollow sphere	64.0 wt%, 6.1 $mg\,cm^{-2}$, 0.3 $mg\,cm^{-2}$	12 $\mu L\,mg^{-1}$	478 $mAh\,g^{-1}$, 86.3%, 300, 0.5 C	1.8–2.7 V	[81]
	Separator	MoS_2/Celgard	Intercalation exfoliation and filtration (constructing nanostructure)	Nanosheet	65.0 wt%, N/A, N/A	N/A	401 $mAh\,g^{-1}$, 49.6%, 600, 0.5 C	1.5–3.0 V	[79]
		$(M\text{-}P/P)_{10}$	Intercalation exfoliation and electrostatic assembly (hybridizing with polar materials)	Nanosheet	60.0 wt%, 1.2 $mg\,cm^{-2}$, 0.1 $mg\,cm^{-2}$	N/A	423 $mAh\,g^{-1}$, 42.0%, 2000, 1 C	1.7–2.6 V	[80]
	Anode	MoS_2-coated Li metal	Sputtering (constructing protective layer)	Nanosheet	33.0 wt%, 3.4 $mg\,cm^{-2}$, N/A	N/A	940 $mAh\,g^{-1}$, 84.0%, 1200, 0.5 C	1.5–3.0 V	[82]

Table 1: Continued.

Classification		Material	Preparation method (design strategies)	Structure characteristics	Sulfur content (wt%), areal sulfur loading (mg cm^{-2}), areal loading on the separator (mg cm^{-2})	Electrolyte dosage (μL mg^{-1})	Retained capacity (mAh g^{-1}), capacity retention (%), cycle number, and rate (C)	Voltage range (V)	Reference
Molybdenum selenide	Cathode	$MoSe_2$@rGO/S	Hydrothermal reaction (hybridizing with carbonaceous materials)	Nanoflake	75.8 wt%, 1.7 mg cm^{-2}, N/A	8 μL mg^{-1}	1086 mAh g^{-1}, 67.5%, 250, 0.25 C	1.65–2.8 V	[83]
		$MoSe_2$/N-rGO/S	Freeze-drying and annealing (constructing nanostructure)	Nanoflake	62.0 wt%, 1.1 mg cm^{-2}, N/A	N/A	887 mAh g^{-1}, 86.3%, 100, 0.2 C	1.8–2.8 V	[84]
Molybdenum nitrides	Cathode	Mesoporous Mo_2N/S	Annealing and etching (constructing nanostructure by silicon template)	Mesoporous framework	48.2 wt%, 1.1 mg cm^{-2}, N/A	N/A	914 mAh g^{-1}, 91.9%, 100, 0.5 C	1.7–2.8 V	[92]
		MoN-NC/S	Annealing and etching (constructing nanostructure by MOF template)	Porous framework	77.0 wt%, 1.5 mg cm^{-2}, N/A	N/A	895 mAh g^{-1}, 71.0%, 100, 0.5 C	1.7–2.8 V	[93]
		Mo_2N/S	Annealing (constructing nanostructure)	Mesoporous nanorod	N/A, 8.0 mg cm^{-2}, N/A	N/A	573 mAh g^{-1}, 57.2%, 100, 0.1 C	1.5–3.0 V	[37]
	Separator	MoN_x	Recrystallization and annealing (constructing nanostructure by salt template)	Nanosheet	73.0 wt%, ~1.4 mg cm^{-2}, 0.4 mg cm^{-2}	N/A	566 mAh g^{-1}, 68.1%, 500, 0.5 C	1.7–2.6 V	[97]
		MoN-G/PP	Hydrothermal reaction and annealing (hybridizing with carbonaceous materials)	Nanosheet	90.0 wt%, 1.2 mg cm^{-2}, N/A	N/A	678 mAh g^{-1}, 63.9%, 500, 0.5 C	1.8–2.8 V	[105]
Molybdenum carbides	Cathode	β-Mo_2C/CNF/S	Electrospinning and annealing (constructing nanostructure)	Porous nanofiber membrane	48.2 wt%, 1.5 mg cm^{-2}, N/A	N/A	767 mAh g^{-1}, 75.4%, 50, 0.1 C	1.7–2.8 V	[106]
		CNT/Mo_2C/S	Electrospinning and annealing (constructing nanostructure)	Porous nanofiber membrane	70.0 wt%, 2.5 mg cm^{-2}, N/A	N/A	718 mAh g^{-1}, 86.0%, 100, 1 C	1.6–3.0 V	[107]
		Mo_2C/C@C/S	Annealing (constructing nanostructure)	Hollow sphere	70.0 wt%, 1.0 mg cm^{-2}, N/A	N/A	652 mAh g^{-1}, 81.5%, 300, 1 C	1.7–2.8 V	[108]
		Mo_2C-C NO/S	Annealing and etching (constructing nanostructure by MOF template)	Porous framework	72.2 wt%, 4.2 mg cm^{-2}, N/A	30 μL mg^{-1}	623 mAh g^{-1}, 77.2%, 100, 0.5 C	1.7–2.8 V	[109]

Table 1: Continued.

Classification		Material	Preparation method (design strategies)	Structure characteristics	Sulfur content (wt%), areal sulfur loading (mg cm^{-2}), areal loading on the separator (mg cm^{-2})	Electrolyte dosage (μL mg^{-1})	Retained capacity (mAh g^{-1}), capacity retention (%), cycle number, and rate (C)	Voltage range (V)	Reference
		Mo_2C NP-CNF/S	Hydrothermal reaction and annealing (constructing nanostructure)	3D nanofiber network	N/A, ~1.8 mg cm^{-2}, N/A	N/A	997 mAh g^{-1}, 86.8%, 200, 0.2 C	1.8–2.6 V	[110]
		MoC_{1-x}/C/S	Annealing (constructing nanostructure)	Nanoflower	N/A, ~0.8 mg cm^{-2}, N/A	N/A	860 mAh g^{-1}, 71.6%, 500, 0.48 C	1.8–2.6 V	[111]
		MoC@N-CNF/S	Freeze-drying and annealing (constructing nanostructure by ice template)	Nanofiber membrane	50.0 wt%, 1.5 mg cm^{-2}, N/A	25 μL mg^{-1}	962 mAh g^{-1}, 80.1%, 100, 0.3 C	1.7–2.8 V	[112]
	Separator	MQD@NG/PP	Freeze-drying and annealing (constructing nanostructure by ice template)	Quantum dots	80.0 wt%, 2.1 mg cm^{-2}, N/A	20 μL mg^{-1}	1146 mAh g^{-1}, 93.2%, 100, 0.2 C	1.7–2.8 V	[113]
Molybdenum phosphides	Cathode	MoP-CNT/S	Reflux and annealing (constructing nanostructure)	3D nanofiber network	72.0 wt%, 6.0 mg cm^{-2}, N/A	5 μL mg^{-1}	830 mAh g^{-1}, N/A, 50, 0.08 C	1.7–2.7 V	[114]
	Separator	MoP/rGO	Hydrothermal reaction and annealing (hybridizing with carbonaceous materials)	Nanosheet	77.0 wt%, 3.9 mg cm^{-2}, 0.4 mg cm^{-2}	N/A	760 mAh g^{-1}, 86.4%, 300, 0.5 C	1.8–2.8 V	[115]
		MoP_2/CNT	Reflux and drop casting (constructing nanostructure)	Nanofiber membrane	N/A, 1.2 mg cm^{-2}, 0.3 mg cm^{-2}	N/A	543 mAh g^{-1}, 87.7%, 500, 0.1 C	1.8–2.6 V	[116]
		MoP@C/N HCSs	Annealing (constructing nanostructure)	Hollow sphere	75.0 wt%, 1.5 mg cm^{-2}, 0.8 mg cm^{-2}	N/A	1185 mAh g^{-1}, 97.3%, 100, 0.2 C	1.7–2.8 V	[117]
Molybdenum metal	Cathode	Mo powder/S	Commercial product	Particle	60.0 wt%, ~1.1 mg cm^{-2}, N/A	N/A	1108 mAh g^{-1}, 95.0%, 130, 0.1 C	1.5–3.0 V	[39]
	Separator	CNT/Mo	Filtration and magnetron sputtering (hybridizing with carbonaceous materials)	Nanofiber membrane	N/A, 7.6 mg cm^{-2}, 0.05 mg cm^{-2}	N/A	621 mAh g^{-1}, 80.0%, 100, 0.2 C	1.7–2.8 V	[118]
Heterojunctions	Cathode	C@SnO_2/TMS/S	Hydrothermal reaction and calcination (hybridizing with polar materials)	Hierarchical nanosheet	N/A, ~2.8 mg cm^{-2}, N/A	N/A	710 mAh g^{-1}, 63.0%, 4000, 5 C	1.7–2.8 V	[70]
		2D MoN-VN/S	Recrystallization and annealing (hybridizing with polar materials by salt template)	2D sheet	58.5 wt%, 3.0 mg cm^{-2}, N/A	N/A	555 mAh g^{-1}, 72.0%, 500, 1 C	1.7–2.8 V	[94]

Table 1: Continued.

Classification		Material	Preparation method (design strategies)	Structure characteristics	Sulfur content (wt%), areal sulfur loading ($mg\,cm^{-2}$), areal loading on the separator ($mg\,cm^{-2}$)	Electrolyte dosage ($\mu L\,mg^{-1}$)	Retained capacity ($mAh\,g^{-1}$), capacity retention (%), cycle number, and rate (C)	Voltage range (V)	Reference
		MoO_2-Mo_3N_2/S	Hydrothermal reaction and annealing (hybridizing with polar materials)	Porous nanobelt	75.0 wt%, 3.2 $mg\,cm^{-2}$, N/A	N/A	451 $mAh\,g^{-1}$, 69.0%, 1000, 0.5 C	1.8–3.0 V	[96]
	Separator	MoO_2-Mo_2N	Annealing (hybridizing with polar materials)	Nanobelt	73.0 wt%, 3.1 $mg\,cm^{-2}$, 0.5 $mg\,cm^{-2}$	7 $\mu L\,mg^{-1}$	790 $mAh\,g^{-1}$, 74.0%, 100, 0.1 C	1.7–2.8 V	[95]
		MoP/MoS_2@C	Annealing (hybridizing with polar materials)	Nanoparticle	70.0 wt%, 2.1 $mg\,cm^{-2}$, N/A	15 $\mu L\,mg^{-1}$	650 $mAh\,g^{-1}$, 59.0%, 500, 1 C	1.7–2.8 V	[119]

In addition to the abovementioned analysis, there are several issues that need future endeavors:

(1) Although many materials have demonstrated catalytic capability on the conversion of LiPSs [133], there is currently a lack of criteria to horizontally evaluate and compare their catalytic performance. Therefore, it is of great importance to take the physicochemical properties of Mo-based materials into consideration. For example, the catalytic capability of MoS_2 is related to their different crystal structures, types of defects, and/or active sites (or facets) exposed. Moreover, the redox potential of sulfur hosts versus lithium was reported to be the key parameter for the adsorption and subsequent conversion of LiPSs [31]. As a result, it is highly necessary to exploit advance in situ/ex situ techniques to identify the role of high-valence Mo atoms during the catalysis

(2) An in-depth understanding of the chemical scission of the S-S bond is necessitated. The conversion of LiPSs accompanied by a series of chemical processes severely depends on the chemical state of the material surface. The coordination state of Mo atoms on the surface of Mo-based materials has a significant impact on the adsorption and catalysis of LiPSs. For instance, Sun et al. revealed that Mo_2C (101) surfaces underwent a sulfurization process during the sulfur loading and the resultant sulfurized Mo_2C showed a similar mechanism of adsorption and catalytic activity to that of TMDs [134]

(3) Material design is believed to be an effective strategy for promoting the performance of Mo-based materials in Li-S batteries (Table 1). For example, the Mo-based materials are expected to have high electronic conductivity, strong affinity to LiPSs (or Li^+), excellent catalytic capability, large specific surface areas, and uniform loading (dispersion) to ensure full utilization of cathode sulfur, efficient capture of LiPSs and subsequent conversion, high energy density, and dendrite-free Li plating. Several strategies that are frequently adopted for improving the performance of Mo-based materials include the introduction of defection/heteroatoms (enriching active sites and enhancing conductivity), the hybridization with conductive carbonaceous materials (e.g., rGO, CNT, and CNF for improving conductivity), the synthesis of hierarchical structures (enlarging active sites and providing physical blockage), and the design of heterostructures (engineering the adsorption and catalytic properties)

(4) It is highly desired to develop a scalable, cost-effective, and environmentally friendly method for synthesizing cathode materials toward the commercialization of Li-S batteries. The state-of-the-art strategies reported in the lab typically involve complicated procedures, expensive equipment, toxic substances (e.g., gases and solvents), and high-temperature calcination, which are unfavorable for mass production. In addition, the low sulfur loading, typically 0.5–2.0 mg cm^{-2} as reported in the literature, further hinders the practical application of Li-S batteries with the target energy density of ~500 W h kg^{-1}

Conflicts of Interest

The authors declare that there is no conflict of interest regarding the publication of this article.

Authors' Contributions

H. Dai, G. Z. Sun, and W. Huang conceived the idea and completed the writing of the manuscript. All other authors contributed to the literature collection and manuscript revision.

Acknowledgments

This work was supported by the National Natural Science Foundation of China (Nos. 21975123 and 61704076), the Natural Science Basic Research Program of Shaanxi (No. 2020JM-092), the Six Talent Peaks Project in Jiangsu Province (No. XCL-024), the Postgraduate Research & Practice Innovation Program of Jiangsu Province (Nos. KYCX20_0997 and SJCX20_0401), and the Fundamental Research Funds for the Central Universities.

References

[1] E. W. Zhao, T. Liu, E. Jónsson et al., "In situ NMR metrology reveals reaction mechanisms in redox flow batteries," *Nature*, vol. 579, no. 7798, pp. 224–228, 2020.

[2] H. Liu, Z. Zhu, Q. Yan et al., "A disordered rock salt anode for fast-charging lithium-ion batteries," *Nature*, vol. 585, no. 7823, pp. 63–67, 2020.

[3] H. Xu, X. Zhao, C. Yu et al., "Mechanistic insight in site-selective and anisotropic etching of Prussian blue analogues toward designable complex architectures for efficient energy storage," *Nanoscale*, vol. 12, no. 20, pp. 11112–11118, 2020.

[4] R. Chen, J. Xue, X. Gao et al., "Jahn-Teller distortions boost the ultrahigh areal capacity and cycling robustness of holey NiMn-hydroxide nanosheets for flexible energy storage devices," *Nanoscale*, vol. 12, no. 43, pp. 22075–22081, 2020.

[5] Y. Feng, H. Dai, L. Liu et al., "Hydrangea-like mesoporous carbon architectures embedded with MnO_x nanoparticles for solid-state asymmetric supercapacitors with enhanced areal capacitance," *International Journal of Electrochemical Science*, vol. 15, no. 1, pp. 6841–6851, 2020.

[6] C. Yu, H. Xu, X. Zhao et al., "Scalable preparation of high performance fibrous electrodes with bio-inspired compact core-fluffy sheath structure for wearable supercapacitors," *Carbon*, vol. 157, pp. 106–112, 2020.

[7] C. Yu, J. An, R. Zhou et al., "Microstructure design of carbonaceous fibers: a promising strategy toward high-performance weaveable/wearable supercapacitors," *Small*, vol. 16, no. 25, article 2000653, 2020.

[8] R. Chen, J. Xue, Y. Gong et al., "Mesh-like vertical structures enable both high areal capacity and excellent rate capability," *Journal of Energy Chemistry*, vol. 53, pp. 226–233, 2021.

[9] Z. Qi and H. Wang, "Advanced thin film cathodes for lithium ion batteries," *Research*, vol. 2020, article 2969510, pp. 1–24, 2020.

[10] R. Li, Y. Zhou, W. Li, J. Zhu, and W. Huang, "Structure engineering in biomass-derived carbon materials for electrochemical energy storage," *Research*, vol. 2020, article 8685436, pp. 1–27, 2020.

[11] Y. Zhang, K. Rui, A. Huang et al., "Stereoassembled V_2O_5@FeOOH hollow architectures with lithiation volumetric strain self-reconstruction for lithium-ion storage," *Research*, vol. 2020, article 2360796, pp. 1–9, 2020.

[12] Z. Tang, S. Wang, J. Liao et al., "Facilitating lithium-ion diffusion in layered cathode materials by introducing Li^+/Ni^{2+} antisite defects for high-rate Li-ion batteries," *Research*, vol. 2019, article 2198906, pp. 1–10, 2019.

[13] T. Sun, Z. Li, and X. Zhang, "Achieving of high density/utilization of active groups via synergic integration of C=N and C=O bonds for ultra-stable and high-rate lithium-ion batteries," *Research*, vol. 2018, article 1936735, 10 pages, 2018.

[14] Y. Mo, J. Liu, S. Wang et al., "Low-carbon and nanosheathed ZnCo2O4Spheroids with porous architecture for boosted lithium storage properties," *Research*, vol. 2019, article 1354829, pp. 1–11, 2019.

[15] J. Guo, J. Liu, H. Dai et al., "Nitrogen doped carbon nanofiber derived from polypyrrole functionalized polyacrylonitrile for applications in lithium-ion batteries and oxygen reduction reaction," *Journal of Colloid and Interface Science*, vol. 507, pp. 154–161, 2017.

[16] X. Zhao, H. Xu, Z. Hui et al., "Electrostatically assembling 2D nanosheets of MXene and MOF-derivatives into 3D hollow frameworks for enhanced lithium storage," *Small*, vol. 15, no. 47, article 1904255, 2019.

[17] J. Balach, J. Linnemann, T. Jaumann, and L. Giebeler, "Metal-based nanostructured materials for advanced lithium-sulfur batteries," *Journal of Materials Chemistry A*, vol. 6, no. 46, pp. 23127–23168, 2018.

[18] D. Wang, Q. Zeng, G. Zhou et al., "Carbon-sulfur composites for Li-S batteries: status and prospects," *Journal of Materials Chemistry A*, vol. 1, no. 33, pp. 9382–9394, 2013.

[19] C. Ye, D. Chao, J. Shan, H. Li, K. Davey, and S. Z. Qiao, "Unveiling the advances of 2D materials for Li/Na-S batteries experimentally and theoretically," *Matter*, vol. 2, no. 2, pp. 323–344, 2020.

[20] J. Xu, T. Lawson, H. Fan, D. Su, and G. Wang, "Updated metal compounds (MOFs, –S, –OH, –N, –C) used as cathode materials for lithium-sulfur batteries," *Advanced Energy Materials*, vol. 8, no. 10, article 1702607, 2018.

[21] G. Zhou, L. Li, D. Wang et al., "A flexible sulfur-graphene-polypropylene separator integrated electrode for advanced Li-S batteries," *Advanced Materials*, vol. 27, no. 4, pp. 641–647, 2015.

[22] T. Ali and C. Yan, "2 D materials for inhibiting the shuttle effect in advanced lithium-sulfur batteries," *ChemSusChem*, vol. 13, no. 6, pp. 1447–1479, 2020.

[23] T. Li, X. Bai, U. Gulzar et al., "A comprehensive understanding of lithium-sulfur battery technology," *Advanced Functional Materials*, vol. 29, no. 32, article 1901730, 2019.

[24] M. Zhang, W. Chen, L. Xue et al., "Adsorption-catalysis design in the lithium-sulfur battery," *Advanced Energy Materials*, vol. 10, no. 2, article 1903008, 2019.

[25] B. Li, H. Peng, X. Chen et al., "Polysulfide electrocatalysis on framework porphyrin in high-capacity and high-stable lithium–sulfur batteries," *CCS Chemistry*, vol. 1, no. 1, pp. 128–137, 2019.

[26] B. Li, X. Chen, X. Chen et al., "Favorable lithium nucleation on lithiophilic framework porphyrin for dendrite-free lithium metal anodes," *Research*, vol. 2019, article 4608940, pp. 1–11, 2019.

[27] D. Liu, C. Zhang, G. Zhou et al., "Catalytic effects in lithium-sulfur batteries: promoted sulfur transformation and reduced shuttle effect," *Advanced Science*, vol. 5, no. 1, article 1700270, 2018.

[28] H. Kim, H. D. Lim, J. Kim, and K. Kang, "Graphene for advanced Li/S and Li/air batteries," *Journal of Materials Chemistry A*, vol. 2, no. 1, pp. 33–47, 2014.

[29] M. Wang, X. Xia, Y. Zhong et al., "Porous carbon hosts for lithium-sulfur batteries," *Chemistry–A European Journal*, vol. 25, no. 15, pp. 3710–3725, 2019.

[30] M. Zheng, Y. Chi, Q. Hu et al., "Carbon nanotube-based materials for lithium-sulfur batteries," *Journal of Materials Chemistry A*, vol. 7, no. 29, pp. 17204–17241, 2019.

[31] X. Liang, C. Y. Kwok, F. Lodi-Marzano et al., "Tuning transition metal oxide-sulfur interactions for long life lithium sulfur batteries: the "Goldilocks" principle," *Advanced Energy Materials*, vol. 6, no. 6, article 1501636, 2016.

[32] X. Liu, J. Huang, Q. Zhang, and L. Mai, "Nanostructured metal oxides and sulfides for lithium-sulfur batteries," *Advanced Materials*, vol. 29, no. 20, article 1601759, 2017.

[33] Y. Zhong, X. Xia, F. Shi, J. Zhan, J. Tu, and H. J. Fan, "Transition metal carbides and nitrides in energy storage and conversion," *Advanced Science*, vol. 3, no. 5, article 1500286, 2016.

[34] K. Tang, S. A. Farooqi, X. Wang, and C. Yan, "Recent progress on molybdenum oxides for rechargeable batteries," *ChemSusChem*, vol. 12, no. 4, pp. 755–771, 2019.

[35] D. Xia, F. Gong, X. Pei et al., "Molybdenum and tungsten disulfides-based nanocomposite films for energy storage and conversion: a review," *Chemical Engineering Journal*, vol. 348, pp. 908–928, 2018.

[36] A. Eftekhari, "Molybdenum diselenide ($MoSe_2$) for energy storage, catalysis, and optoelectronics," *Applied Materials Today*, vol. 8, pp. 1–17, 2017.

[37] N. Mosavati, S. O. Salley, and K. Y. S. Ng, "Characterization and electrochemical activities of nanostructured transition metal nitrides as cathode materials for lithium sulfur batteries," *Journal of Power Sources*, vol. 340, pp. 210–216, 2017.

[38] X. Chen, X. Ding, C. Wang et al., "A multi-shelled CoP nanosphere modified separator for highly efficient Li-S batteries," *Nanoscale*, vol. 10, no. 28, pp. 13694–13701, 2018.

[39] X. Liu, S. P. Zhou, M. Liu et al., "Utilizing a metal as a sulfur host for high performance Li-S batteries," *Nano Energy*, vol. 50, pp. 685–690, 2018.

[40] I. A. de Castro, R. S. Datta, J. Z. Ou et al., "Molybdenum oxides–from fundamentals to functionality,," *Advanced Materials*, vol. 29, no. 40, article 1701619, 2017.

[41] Q. Xia, H. Zhao, Z. du et al., "Facile synthesis of MoO_3/carbon nanobelts as high- performance anode material for lithium ion batteries," *Electrochimica Acta*, vol. 180, pp. 947–956, 2015.

[42] R. Wu, H. Xu, Y. Zhao et al., "Borophene-like boron subunits-inserted molybdenum framework of MoB_2 enables

stable and quick-acting Li_2S_6-based lithium-sulfur batteries," *Energy Storage Materials*, vol. 32, pp. 216–224, 2020.

[43] F. Xie, W. C. Choy, C. Wang, X. Li, S. Zhang, and J. Hou, "Low-temperature solution-processed hydrogen molybdenum and vanadium bronzes for an efficient hole-transport layer in organic electronics," *Advanced Materials*, vol. 25, no. 14, pp. 2051–2055, 2013.

[44] C. Freund, M. Abrantes, and F. E. Kühn, "Monomeric cyclopentadiene molybdenum oxides and their carbonyl precursors as epoxidation catalysts," *Journal of Organometallic Chemistry*, vol. 691, no. 18, pp. 3718–3729, 2006.

[45] G. Zhang, T. Xiong, M. Yan et al., "α-MoO_{3-x} by plasma etching with improved capacity and stabilized structure for lithium storage," *Nano Energy*, vol. 49, pp. 555–563, 2018.

[46] H. Li, L. McRae, C. J. Firby, and A. Y. Elezzabi, "Rechargeable aqueous electrochromic batteries utilizing Ti-substituted tungsten molybdenum oxide based Zn^{2+} Ion intercalation cathodes," *Advanced Materials*, vol. 31, no. 15, article 1807065, 2019.

[47] Y. Yi, H. An, P. Zhang et al., "Oxygen deficiency driven conversion of polysulfide by electrocatalysis: MoO3-x nanobelts for an improved lithium-sulfur battery cathode," *ChemNanoMat*, vol. 5, no. 7, pp. 926–931, 2019.

[48] W. Yang, J. Xiao, Y. Ma et al., "Tin intercalated ultrathin MoO_3 Nanoribbons for advanced lithium-sulfur batteries," *Advanced Energy Materials*, vol. 9, no. 7, article 1803137, 2019.

[49] L. Huang, B. Yao, J. Sun et al., "Highly conductive and flexible molybdenum oxide nanopaper for high volumetric supercapacitor electrode," *Journal of Materials Chemistry A*, vol. 5, no. 6, pp. 2897–2903, 2017.

[50] Q. Zhang, Y. Wang, Z. W. Seh, Z. Fu, R. Zhang, and Y. Cui, "Understanding the anchoring effect of two-dimensional layered materials for lithium-sulfur batteries," *Nano Letters*, vol. 15, no. 6, pp. 3780–3786, 2015.

[51] Y. Jing, Q. Pan, Z. Cheng, X. Dong, and Y. Xiang, "Direct thermal intercalation of amine into layered MoO_3," *Materials Science and Engineering: B*, vol. 138, no. 1, pp. 55–59, 2007.

[52] D. Chen, X. Yue, X. Li et al., "Freestanding double-layer MoO_3/CNT@S membrane: a promising flexible cathode for lithium-sulfur batteries," *ACS Applied Materials & Interfaces*, vol. 12, no. 2, pp. 2354–2361, 2020.

[53] S. Imtiaz, Z. Ali Zafar, R. Razaq et al., "Electrocatalysis on separator modified by molybdenum trioxide nanobelts for lithium-sulfur batteries," *Advanced Materials Interfaces*, vol. 5, no. 15, article 1800243, 2018.

[54] L. Luo, X. Qin, J. Wu et al., "An interwoven MoO_3@CNT scaffold interlayer for high-performance lithium-sulfur batteries," *Journal of Materials Chemistry A*, vol. 6, no. 18, pp. 8612–8619, 2018.

[55] H. Li, X. Wang, C. Qi et al., "Self-assembly of MoO_3-decorated carbon nanofiber interlayers for high-performance lithium-sulfur batteries," *Physical Chemistry Chemical Physics*, vol. 22, no. 4, pp. 2157–2163, 2020.

[56] D. Zhu, T. Long, B. Xu et al., "Recent advances in interlayer and separator engineering for lithium-sulfur batteries," *Journal of Energy Chemistry*, vol. 57, pp. 41–60, 2021.

[57] N. Kaisar, S. A. Abbas, J. Ding et al., "A lithium passivated MoO3nanobelt decorated polypropylene separator for fast-charging long-life Li-S batteries," *Nanoscale*, vol. 11, no. 6, pp. 2892–2900, 2019.

[58] L. Mai, B. Hu, W. Chen et al., "Lithiated MoO_3 nanobelts with greatly improved performance for lithium batteries," *Advanced Materials*, vol. 19, no. 21, pp. 3712–3716, 2007.

[59] X. Wu, Y. du, P. Wang et al., "Kinetics enhancement of lithium-sulfur batteries by interlinked hollow MoO_2 sphere/-nitrogen-doped graphene composite," *Journal of Materials Chemistry A*, vol. 5, no. 48, pp. 25187–25192, 2017.

[60] C. Wang, K. Li, F. Zhang, Z. Wu, L. Sun, and L. Wang, "Insight of enhanced redox chemistry for porous MoO2 carbon-derived framework as polysulfide reservoir in lithium-sulfur batteries," *ACS Applied Materials & Interfaces*, vol. 10, no. 49, pp. 42286–42293, 2018.

[61] T. Ressler, "Bulk structural investigation of the reduction of MoO_3 with propene and the oxidation of MoO_2 with oxygen," *Journal of Catalysis*, vol. 210, no. 1, pp. 67–83, 2002.

[62] R. Razaq, D. Sun, Y. Xin et al., "Nanoparticle assembled mesoporous MoO_2 Microrods derived from metal organic framework and wrapped with graphene as the sulfur host for long-life lithium-sulfur batteries," *Advanced Materials Interfaces*, vol. 6, no. 4, article 1801636, 2019.

[63] R. Zhuang, S. Yao, X. Shen, and T. Li, "A freestanding MoO_2-decorated carbon nanofibers interlayer for rechargeable lithium sulfur battery," *International Journal of Energy Research*, vol. 43, no. 3, pp. 1111–1120, 2019.

[64] W. Kong, L. Yan, Y. Luo et al., "Ultrathin MnO_2/graphene oxide/carbon nanotube interlayer as efficient polysulfide-trapping shield for high-performance Li-S batteries," *Advanced Functional Materials*, vol. 27, no. 18, article 1606663, 2017.

[65] K. Huang, J. Zhang, G. Shi, and Y. Liu, "Hydrothermal synthesis of molybdenum disulfide nanosheets as supercapacitors electrode material," *Electrochimica Acta*, vol. 132, pp. 397–403, 2014.

[66] H. Li, Q. Zhang, C. C. R. Yap et al., "From bulk to monolayer MoS_2: evolution of Raman scattering," *Advanced Functional Materials*, vol. 22, no. 7, pp. 1385–1390, 2012.

[67] F. R. Fan and W. Wu, "Emerging devices based on two-dimensional monolayer materials for energy harvesting," *Research*, vol. 2019, article 7367828, pp. 1–16, 2019.

[68] C. Yu, H. Xu, Y. Sun et al., "The incorporation of expanded 1T-enriched MoS_2 boosts hybrid fiber improved charge storage capability," *Carbon*, vol. 170, pp. 543–549, 2020.

[69] G. Babu, N. Masurkar, H. Al Salem, and L. M. Arava, "Transition metal dichalcogenide atomic layers for lithium polysulfides electrocatalysis," *Journal of the American Chemical Society*, vol. 139, no. 1, pp. 171–178, 2017.

[70] M. Wang, L. Fan, D. Tian et al., "Rational design of hierarchical SnO2/1T-MoS2 nanoarray electrode for ultralong-life Li-S batteries," *ACS Energy Letters*, vol. 3, no. 7, pp. 1627–1633, 2018.

[71] H. Lin, L. Yang, X. Jiang et al., "Electrocatalysis of polysulfide conversion by sulfur-deficient MoS2nanoflakes for lithium-sulfur batteries," *Energy & Environmental Science*, vol. 10, no. 6, pp. 1476–1486, 2017.

[72] H. Lin, S. Zhang, T. Zhang et al., "Simultaneous cobalt and phosphorous doping of MoS_2 for improved catalytic performance on polysulfide conversion in lithium–sulfur batteries," *Advanced Energy Materials*, vol. 9, no. 38, article 1902096, 2019.

[73] X. Li and H. Zhu, "Two-dimensional MoS_2: properties, preparation, and applications," *Journal of Materiomics*, vol. 1, no. 1, pp. 33–44, 2015.

[74] W. Zhou, Z. Yin, Y. du et al., "Synthesis of few-layer MoS_2 Nanosheet-Coated TiO_2 Nanobelt heterostructures for enhanced photocatalytic activities," *Small*, vol. 9, no. 1, pp. 140–147, 2013.

[75] J. Xie, H. Zhang, S. Li et al., "Defect-rich MoS_2 ultrathin nanosheets with additional active edge sites for enhanced electrocatalytic hydrogen evolution," *Advanced Materials*, vol. 25, no. 40, pp. 5807–5813, 2013.

[76] J. Jiang, T. Xu, J. Lu, L. Sun, and Z. Ni, "Defect engineering in 2D materials: precise manipulation and improved functionalities," *Research*, vol. 2019, article 4641739, pp. 1–14, 2019.

[77] Z. Zheng, H. Guo, F. Pei et al., "High sulfur loading in hierarchical porous carbon rods constructed by vertically oriented porous graphene-like nanosheets for Li-S batteries," *Advanced Functional Materials*, vol. 26, no. 48, pp. 8952–8959, 2016.

[78] M. Liu, C. Zhang, J. Su et al., "Propelling polysulfide conversion by defect-rich MoS2 nanosheets for high-performance lithium-sulfur batteries," *ACS Applied Materials & Interfaces*, vol. 11, no. 23, pp. 20788–20795, 2019.

[79] Z. A. Ghazi, X. He, A. M. Khattak et al., "MoS_2/Celgard separator as efficient polysulfide barrier for long-life lithium-sulfur batteries," *Advanced Materials*, vol. 29, no. 21, article 1606817, 2017.

[80] J. Wu, H. Zeng, X. Li et al., "Ultralight layer-by-layer self-assembled MoS_2-polymer modified separator for simultaneously trapping polysulfides and suppressing lithium dendrites," *Advanced Energy Materials*, vol. 8, no. 35, article 1802430, 2018.

[81] N. Zheng, G. Jiang, X. Chen, J. Mao, N. Jiang, and Y. Li, "Battery separators functionalized with edge-rich MoS_2/C hollow microspheres for the uniform deposition of Li_2S in high-performance lithium-sulfur batteries," *Nano-Micro Letters*, vol. 11, 2019.

[82] E. Cha, M. D. Patel, J. Park et al., "2D MoS_2 as an efficient protective layer for lithium metal anodes in high-performance Li-S batteries," *Nature Nanotechnology*, vol. 13, no. 4, pp. 337–344, 2018.

[83] H. Wong, X. Ou, M. Zhuang et al., "Selenium edge as a selective anchoring site for lithium-sulfur batteries with $MoSe_2$/graphene-based cathodes," *ACS Applied Materials & Interfaces*, vol. 11, no. 22, pp. 19986–19993, 2019.

[84] W. Tian, B. Xi, Z. Feng, H. Li, J. Feng, and S. Xiong, "Sulfiphilic few-layered $MoSe_2$ Nanoflakes decorated rGO as a highly efficient sulfur host for lithium-sulfur batteries," *Advanced Energy Materials*, vol. 9, no. 36, article 1901896, 2019.

[85] Y. Liu, M. Zhu, and D. Chen, "Sheet-like $MoSe_2$/C composites with enhanced Li-ion storage properties," *Journal of Materials Chemistry A*, vol. 3, no. 22, pp. 11857–11862, 2015.

[86] S. Han, K. Zhou, Y. Yu et al., "A general method for the synthesis of hybrid nanostructures using $MoSe_2$ Nanosheet-Assembled nanospheres as templates," *Research*, vol. 2019, article 6439734, pp. 1–10, 2019.

[87] Q. Hao, G. Cui, Y. Zhang, J. Li, and Z. Zhang, "Novel $MoSe_2$/-MoO_2 heterostructure as an effective sulfur host for high-performance lithium/sulfur batteries," *Chemical Engineering Journal*, vol. 381, article 122672, 2020.

[88] Y. Abghoui and E. Skúlason, "Hydrogen evolution reaction catalyzed by transition-metal nitrides," *The Journal of Physical Chemistry C*, vol. 121, no. 43, pp. 24036–24045, 2017.

[89] C. Q. YI, J. P. ZOU, H. Z. YANG, and X. LENG, "Recent advances in pseudocapacitor electrode materials: transition metal oxides and nitrides," *Transactions of Nonferrous Metals Society of China*, vol. 28, no. 10, pp. 1980–2001, 2018.

[90] M. Zhao, H. Peng, B. Li et al., "Electrochemical phase evolution of metal-based pre-catalysts for high-rate polysulfide conversion," *Angewandte Chemie International Edition*, vol. 59, no. 23, pp. 9011–9017, 2020.

[91] L. Lan, D. Chen, Y. Yao et al., "Phase-dependent fluorescence quenching efficiency of MoS2 nanosheets and their applications in multiplex target biosensing," *ACS Applied Materials & Interfaces*, vol. 10, no. 49, pp. 42009–42017, 2018.

[92] G. Jiang, F. Xu, S. Yang, J. Wu, B. Wei, and H. Wang, "Mesoporous, conductive molybdenum nitride as efficient sulfur hosts for high- performance lithium-sulfur batteries," *Journal of Power Sources*, vol. 395, pp. 77–84, 2018.

[93] P. Wang, N. Li, Z. Zhang et al., "Synergetic enhancement of polysulfide chemisorption and electrocatalysis over bicontinuous MoN@N-rich carbon porous nano-octahedra for Li-S batteries," *Journal of Materials Chemistry A*, vol. 7, no. 38, pp. 21934–21943, 2019.

[94] C. Ye, Y. Jiao, H. Jin et al., "2D MoN-VN heterostructure to regulate polysulfides for highly efficient lithium-sulfur batteries," *Angewandte Chemie International Edition*, vol. 57, no. 51, pp. 16703–16707, 2018.

[95] J. Yang, S. Zhao, Y. Lu, X. T. Zeng, W. Lv, and G. Z. Cao, "In-situ topochemical nitridation derivative MoO_2-Mo_2N binary nanobelts as multifunctional interlayer for fast-kinetic Li-sulfur batteries," *Nano Energy*, vol. 68, article 104356, 2020.

[96] R. Li, X. Zhou, H. Shen, M. Yang, and C. Li, "Conductive holey MoO2–Mo3N2 heterojunctions as job-synergistic cathode host with low surface area for high-loading Li-S batteries," *ACS Nano*, vol. 13, no. 9, pp. 10049–10061, 2019.

[97] G. Chen, X. Song, S. Wang, X. Chen, and H. Wang, "Two-dimensional molybdenum nitride nanosheets modified Celgard separator with multifunction for Li S batteries," *Journal of Power Sources*, vol. 408, pp. 58–64, 2018.

[98] L. Luo, J. Li, H. Yaghoobnejad Asl, and A. Manthiram, "A 3D lithiophilic Mo_2N-modified carbon nanofiber architecture for dendrite-free lithium-metal anodes in a full cell," *Advanced Materials*, vol. 31, no. 48, article 1904537, 2019.

[99] R. Zhang, M. Wu, X. Fan, H. Jiang, and T. Zhao, "Superior cycling life of Li-S batteries with high sulfur loading enabled by a bifunctional layered-MoO_3 cathode," *Journal of Power Sources*, vol. 436, p. 226840, 2019.

[100] Q. Qu, T. Gao, H. Zheng et al., "Strong surface-bound sulfur in conductive MoO_2 Matrix for enhancing Li-S battery performance," *Advanced Materials Interfaces*, vol. 2, no. 7, article 1500048, 2015.

[101] H. Wei, Y. Ding, H. Li et al., "MoS_2 quantum dots decorated reduced graphene oxide as a sulfur host for advanced lithium-sulfur batteries," *Electrochimica Acta*, vol. 327, p. 134994, 2019.

[102] W. Tang, Z. Chen, B. Tian et al., "In situ observation and electrochemical study of encapsulated sulfur nanoparticles by MoS2 flakes," *Journal of the American Chemical Society*, vol. 139, no. 29, pp. 10133–10141, 2017.

[103] L. Yan, N. Luo, W. Kong et al., "Enhanced performance of lithium-sulfur batteries with an ultrathin and lightweight MoS_2/carbon nanotube interlayer," *Journal of Power Sources*, vol. 389, pp. 169–177, 2018.

[104] S. Majumder, M. Shao, Y. Deng, and G. Chen, "Ultrathin sheets of MoS_2/g-C_3N_4 composite as a good hosting material of sulfur for lithium-sulfur batteries," *Journal of Power Sources*, vol. 431, pp. 93–104, 2019.

[105] D. Tian, X. Song, M. Wang et al., "MoN supported on graphene as a bifunctional interlayer for advanced Li-S batteries," *Advanced Energy Materials*, vol. 9, no. 46, article 1901940, 2019.

[106] R. Zhuang, S. Yao, X. Shen, T. Li, S. Qin, and J. Yang, "Electrospun β-Mo_2C/CNFs as an efficient sulfur host for rechargeable lithium sulfur battery," *Journal of Materials Science: Materials in Electronics*, vol. 30, no. 5, pp. 4626–4633, 2019.

[107] C. Shang, L. Cao, M. Yang et al., "Freestanding Mo_2C-decorating N-doped carbon nanofibers as 3D current collector for ultra-stable Li-S batteries," *Energy Storage Materials*, vol. 18, pp. 375–381, 2019.

[108] Z. Wang, X. Xu, Z. Liu, S. Ji, S. O. Ahmed Idris, and J. Liu, "Hollow spheres of Mo_2C@C as synergistically confining sulfur host for superior Li–S battery cathode," *Electrochimica Acta*, vol. 332, article 135482, 2020.

[109] G. Chen, Y. Li, W. Zhong et al., "MOFs-derived porous Mo_2C-C nano-octahedrons enable high- performance lithium-sulfur batteries," *Energy Storage Materials*, vol. 25, pp. 547–554, 2020.

[110] F. Zhou, Z. Li, X. Luo et al., "Low cost metal carbide nanocrystals as binding and electrocatalytic sites for high performance Li-S batteries," *Nano Letters*, vol. 18, no. 2, pp. 1035–1043, 2018.

[111] Y. Wu, J. Deng, Y. Zhou, Y. Huang, and Y. Li, "Molybdenum carbide nanostructures for electrocatalytic polysulfide conversion in lithium-polysulfide batteries," *Nanoscale Horizons*, vol. 5, no. 3, pp. 501–506, 2020.

[112] H. Shi, Z. Sun, W. Lv et al., "Necklace-like MoC sulfiphilic sites embedded in interconnected carbon networks for Li-S batteries with high sulfur loading," *Journal of Materials Chemistry A*, vol. 7, no. 18, pp. 11298–11304, 2019.

[113] B. Yu, D. Chen, Z. Wang et al., "Mo_2C quantum dots@graphene functionalized separator toward high-current-density lithium metal anodes for ultrastable Li-S batteries," *Chemical Engineering Journal*, vol. 399, p. 125837, 2020.

[114] Y. Mi, W. Liu, X. Li, J. Zhuang, H. Zhou, and H. Wang, "High-performance Li-S battery cathode with catalyst-like carbon nanotube-MoP promoting polysulfide redox," *Nano Research*, vol. 10, no. 11, pp. 3698–3705, 2017.

[115] M. Li, C. Wang, L. Miao et al., "A separator-based lithium polysulfide recirculator for high-loading and high-performance Li-S batteries," *Journal of Materials Chemistry A*, vol. 6, no. 14, pp. 5862–5869, 2018.

[116] Y. Luo, N. Luo, W. Kong et al., "Multifunctional interlayer based on molybdenum diphosphide catalyst and carbon nanotube film for lithium-sulfur batteries," *Small*, vol. 14, no. 8, article 1702853, 2018.

[117] Z. Sun, X. L. Wu, Z. Peng et al., "Compactly coupled nitrogen-doped carbon nanosheets/molybdenum phosphide nanocrystal hollow nanospheres as polysulfide reservoirs for high-performance lithium-sulfur chemistry," *Small*, vol. 15, no. 40, article 1902491, 2019.

[118] Y. Li, C. Wang, W. Wang et al., "Enhanced chemical immobilization and catalytic conversion of polysulfide intermediates using metallic Mo nanoclusters for high-performance Li-S batteries," *ACS Nano*, vol. 14, no. 1, pp. 1148–1157, 2020.

[119] J. Zhang, J. Zhang, K. Liu et al., "Abundant defects-induced interfaces enabling effective anchoring for polysulfides and enhanced kinetics in lean electrolyte lithium-sulfur batteries," *ACS Applied Materials & Interfaces*, vol. 11, no. 50, pp. 46767–46775, 2019.

[120] R. Razaq, D. Sun, Y. Xin et al., "Enhanced kinetics of polysulfide redox reactions on Mo_2C/CNT in lithium-sulfur batteries," *Nanotechnology*, vol. 29, no. 29, article 295401, 2018.

[121] X. Zhou, L. Li, J. Yang, L. Xu, and J. Tang, "Cobalt and molybdenum carbide nanoparticles grafted on nitrogen-doped carbon nanotubes as efficient chemical anchors and polysulfide conversion catalysts for lithium-sulfur batteries," *ChemElectroChem*, vol. 7, no. 18, pp. 3767–3775, 2020.

[122] S. T. Oyama, "Novel catalysts for advanced hydroprocessing: transition metal phosphides," *Journal of Catalysis*, vol. 216, no. 1–2, pp. 343–352, 2003.

[123] Y. Wang, B. Kong, D. Zhao, H. Wang, and C. Selomulya, "Strategies for developing transition metal phosphides as heterogeneous electrocatalysts for water splitting," *Nano Today*, vol. 15, pp. 26–55, 2017.

[124] Y. Teng, A. Wang, X. Li, J. Xie, Y. Wang, and Y. Hu, "Preparation of high-performance MoP hydrodesulfurization catalysts via a sulfidation-reduction procedure," *Journal of Catalysis*, vol. 266, no. 2, pp. 369–379, 2009.

[125] J. Bai, X. Li, A. Wang, R. Prins, and Y. Wang, "Hydrodesulfurization of dibenzothiophene and its hydrogenated intermediates over bulk MoP," *Journal of Catalysis*, vol. 287, pp. 161–169, 2012.

[126] Y. Yang, Y. Zhong, Q. Shi, Z. Wang, K. Sun, and H. Wang, "Electrocatalysis in lithium sulfur batteries under lean electrolyte conditions," *Angewandte Chemie International Edition*, vol. 57, no. 47, pp. 15549–15552, 2018.

[127] F. Ma, X. Wang, J. Wang et al., "Phase-transformed Mo_4P_3 nanoparticles as efficient catalysts towards lithium polysulfide conversion for lithium-sulfur battery," *Electrochimica Acta*, vol. 330, p. 135310, 2020.

[128] H. Jin, X. Liu, S. Chen et al., "Heteroatom-doped transition metal electrocatalysts for hydrogen evolution reaction," *ACS Energy Letters*, vol. 4, no. 4, pp. 805–810, 2019.

[129] J. Wang, Q. Wang, W. She et al., "Tuning the electron density distribution of the Co-N-C catalysts through guest molecules and heteroatom doping to boost oxygen reduction activity," *Journal of Power Sources*, vol. 418, pp. 50–60, 2019.

[130] T. Liu, J. Wang, C. Zhong et al., "Benchmarking three ruthenium phosphide phases for electrocatalysis of the hydrogen evolution reaction: experimental and theoretical insights," *Chemistry–A European Journal*, vol. 25, no. 33, pp. 7826–7830, 2019.

[131] Y. Wang, J. Wang, T. Xie et al., "Ru doping in $Ni(OH)_2$ to accelerate water reduction kinetics for efficient hydrogen evolution reaction," *Applied Surface Science*, vol. 485, pp. 506–512, 2019.

[132] K. Vasu, O. E. Meiron, A. N. Enyashin, R. Bar-Ziv, and M. Bar-Sadan, "Effect of Ru doping on the properties of

$MoSe_2$ nanoflowers," *The Journal of Physical Chemistry C*, vol. 123, no. 3, pp. 1987–1994, 2018.

[133] W. G. Lim, S. Kim, C. Jo, and J. Lee, "A comprehensive review of materials with catalytic effects in Li-S batteries: enhanced redox kinetics," *Angewandte Chemie International Edition*, vol. 58, no. 52, pp. 18746–18757, 2019.

[134] M. Sun, Z. Wang, X. Li et al., "Rational understanding of the catalytic mechanism of molybdenum carbide in polysulfide conversion in lithium-sulfur batteries," *Journal of Materials Chemistry A*, vol. 8, no. 23, pp. 11818–11823, 2020.